Supporting Information for

Sub-decadal Volcanic Tsunamis Due to Submarine Trapdoor Faulting at Sumisu Caldera in the Izu-Bonin Arc

Osamu Sandanbata,[1,2†] Shingo Watada,[1] Kenji Satake,[1] Hiroo Kanamori,[3] Luis Rivera,[4] and Zhongwen Zhan[3]

[1]Earthquake Research Institute, the University of Tokyo, Bunkyo, Tokyo, Japan.

[2]National Research Institute for Earth Science and Disaster Resilience, Tsukuba, Ibaraki, Japan.

[3]Seismological Laboratory, California Institute of Technology, Pasadena, CA 91125, USA.

[4]Université de Strasbourg, CNRS, ITES UMR 7063, Strasbourg F-67084, France.

Corresponding author: Osamu Sandanbata (osm3@bosai.go.jp)

Contents of this file

Text S1 to S3
Figures S1 to S21
Tables S1 to S3
Supplementary References

Additional Supporting Information (Files uploaded separately)

Captions for Data Set S1

Introduction

Supporting information contains descriptions of procedures for the moment tensor analysis (Text S1), and source model variations when we assume low rigidity at the source depth (Text S2) or nonuniform dip angle of the ring fault (Text S3). Supplementary figures and tables mentioned in Main Text and Supplementary Texts (Figures S1 to S21; Tables S1 to S3), and a caption for the supplementary dataset of the source models (Data Set S1), are also contained.

Text S1. Moment tensor analysis

　　We perform the deviatoric moment tensor analysis using the W-phase of seismic waves (Kanamori and Rivera 2008; Duputel et al. 2012; Hayes, Rivera, and Kanamori 2009) for the four earthquakes in 1996, 2006, 2015, and 2018 at Sumisu caldera; we do not analyze the 1984 event, due to inaccessibility of good quality seismic data. We download broad-band seismic records of F-net and/or GSN within the epicentral distances of 30°. We use the same Green's functions of seismic waveforms, the same filter, and assume the same centroid location, as done for the computation of the long-period seismic waveforms in Main Text (see Section 4.3). We assume the zero-trace condition $M_{rr} + M_{\theta\theta} + M_{\phi\phi} = 0$. The optimum time-shift and half duration are assumed to be the same and determined by the grid-search method. In the inversion process, we remove clearly bad records yielding a single-record seismic misfit larger than 1.5 (Table S2). The estimated deviatoric moment tensors are shown in Table S3.

　　From the deviatoric moment tensors, we obtain the *resolvable moment tensors* $\boldsymbol{M_{res}}$, by excluding two elements $M_{r\theta}$ and $M_{r\phi}$ that are indeterminate from long-period seismic data (Sandanbata et al. 2021). $\boldsymbol{M_{res}}$ of the four earthquakes are shown in Figures 10a–d, and their seismograms are shown in Figures S17–S20. Following our previous study (Sandanbata et al. 2021), we examine the dominancy of the vertical-CLVD component (denoted by k_{CLVD}) and the null-axis direction (denoted by the best-fit double-couple orientation) of $\boldsymbol{M_{res}}$. Since the two parameters are controlled by the ring fault arc length and orientation, comparisons of those for the repeating earthquakes enable us to evaluate similarities in their ring fault geometries (See Section 6.3).

Text S2. Effect of a low-rigidity crust on our estimation of the ring fault dip angle

　　In the source modeling in Main Text, we estimated the ring fault dip angle as 85.0°, by utilizing the sensitivity of the long-period seismic amplitudes to the parameter, when we used the velocity model with V_p = 6.0 km/s, V_s = 3.5 km/s, respectively and ρ_0 = 2.6 x 10^3 kg/m^3 in the shallowest crust at < 15 km depth, and assumed the Lamé's constants of λ = 29.9 GPa and μ = 31.85 GPa (see Section 4.3). However, a previous study (Kodaira et al. 2007) suggested a lower-velocity layer with V_p of 1.8–5.8 km/s exists in the shallowest depth < ~5 km of the Izu-Bonin arc, including the region around Sumisu caldera. The low rigidity at the source may reduce the seismic amplitude and thereby affect our estimate of the ring fault dip angle. Here, we estimate an optimal dip angle considering this effect, by computing moment tensors assuming lower values for the Lamé's constants (λ = 9.97 GPa and μ = 10.6 GPa) in the long-period seismic waveform computations. Figure S21 demonstrates that the model with 77° yields the best agreement with the observed seismic amplitude. Thus, if we assume the value of λ and μ ranging from ~10 GPa to ~30 GPa in the shallowest crust, our estimation of the ring fault dip angle ranges from ~77° to ~85°.

**Text S3. Source model with modification of the ring fault dip angle**

　　For an additional analysis, we perform the same earthquake source modeling procedures (see Section 4) for a source structure containing a ring fault along the 2/3-

ring arc length with *nonuniform dip angles* that decrease from 87° on the northeastern part to 83° on the two ends (Figure S15). The source model with this structure inverted from the tsunami waveform data (Figures S15b–c) yields even better seismic waveform fit with a smaller misfit of 0.414 (Figures S16) than the best-fit source model with the uniform ring fault dip angle (seismic misfit of 0.425; Figure 7); for example, the waveform fits of the BHE channel of KZS, YMZ, TYS, and AMM are improved by the minimal parameter tuning.
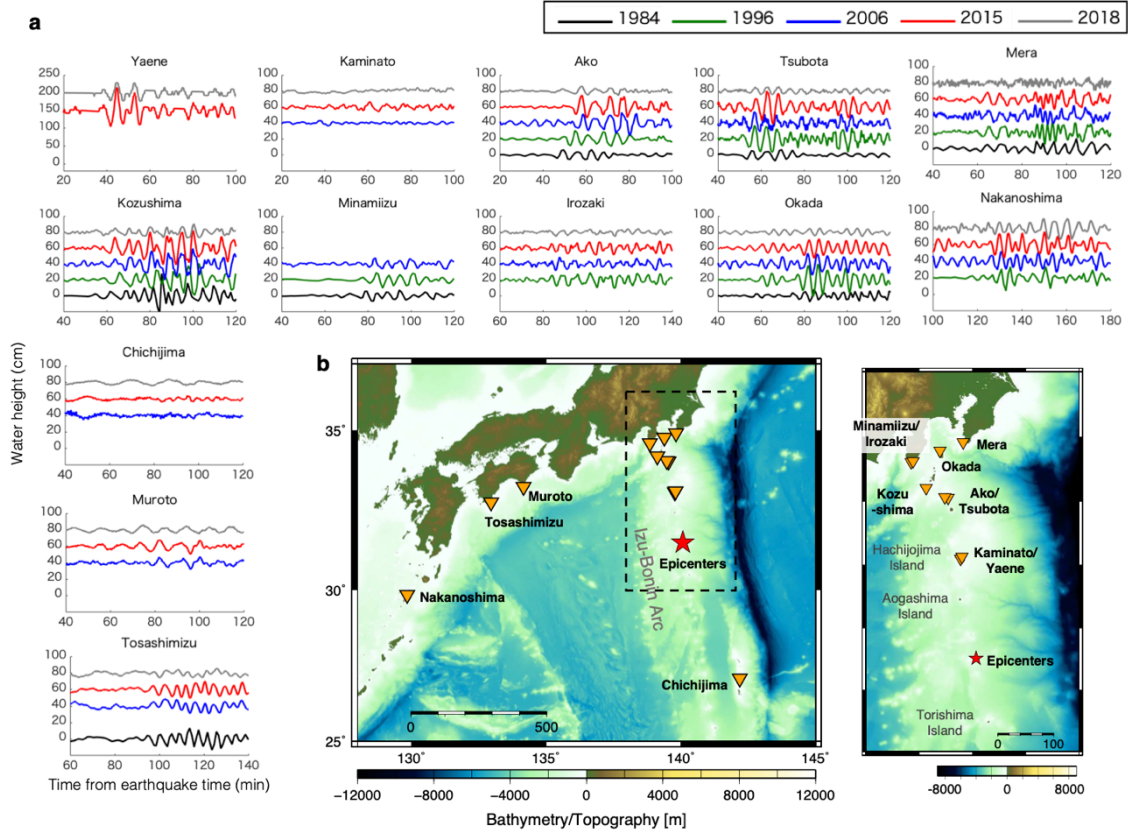
Figure S1. (**a**) Tsunami waveforms from the repeating earthquakes recorded at tide gauge stations shown in **b**. In **a**, base lines for different events are shifted by multiples of 50 cm and 20 cm in the y-axis direction for Yaene and the others, respectively. We remove the tidal trends from the raw data by the polynomial fitting. We additionally apply a band-pass filter (0.001-0.01 Hz) to the records of Tosashimizu and Chichijima to remove noise. Some records of the 1984 and 1996 events are digitized from analogue records. In **b**, red star and orange triangles represent the location of Sumisu caldera where the earthquakes occurred and tide gauge stations, respectively.
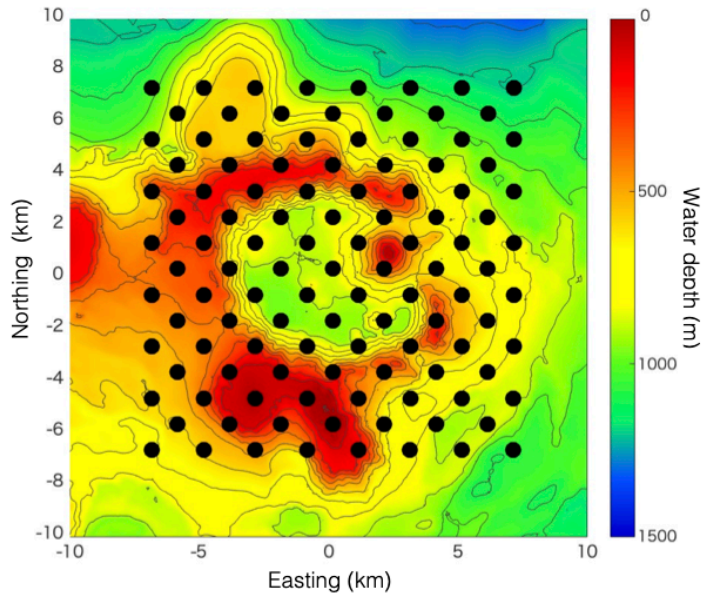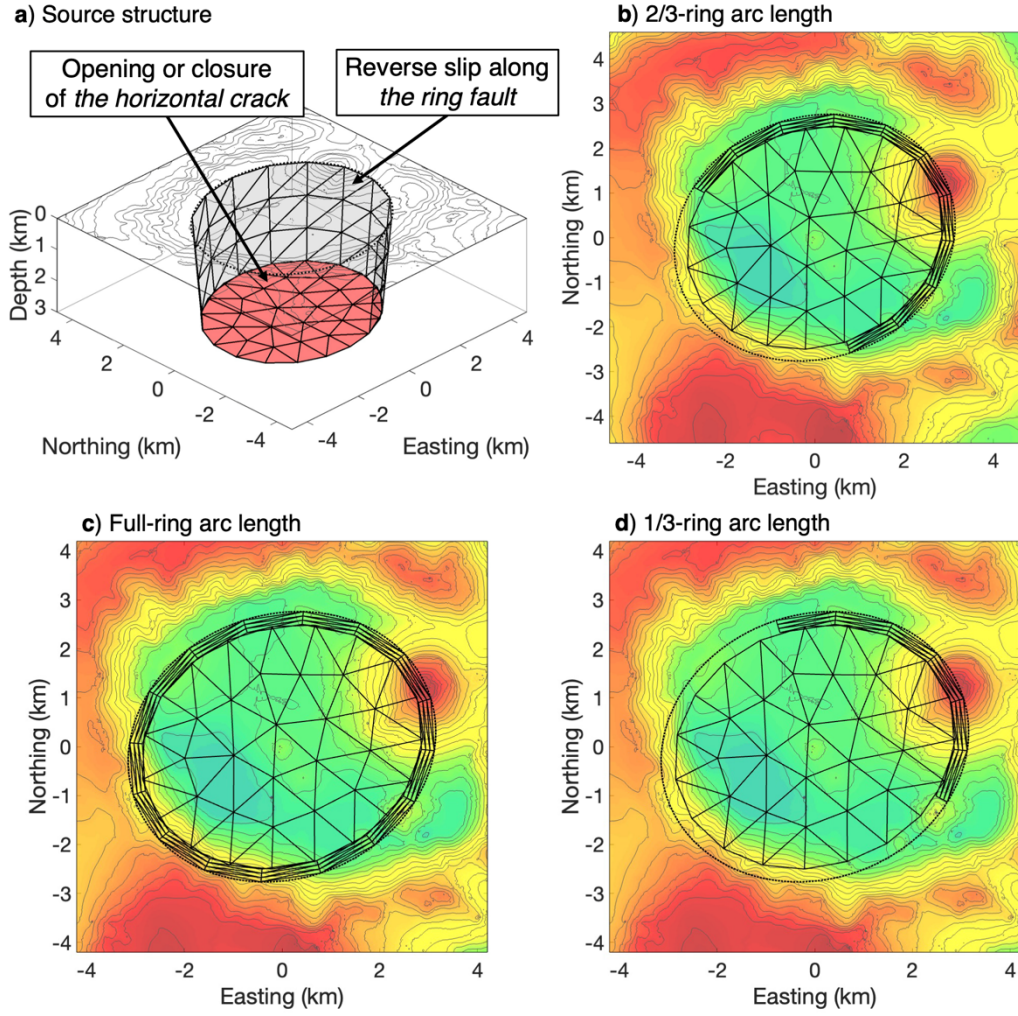
Figure S2. Unit sources of sea-surface displacement. Black dots represent central locations of 113 unit sources on the sea surface to compute the synthetic tsunami waveforms g_j^k; each unit source has a cosine-tapered shape with a horizontal source size of 4 km x 4 km (Equation 1).
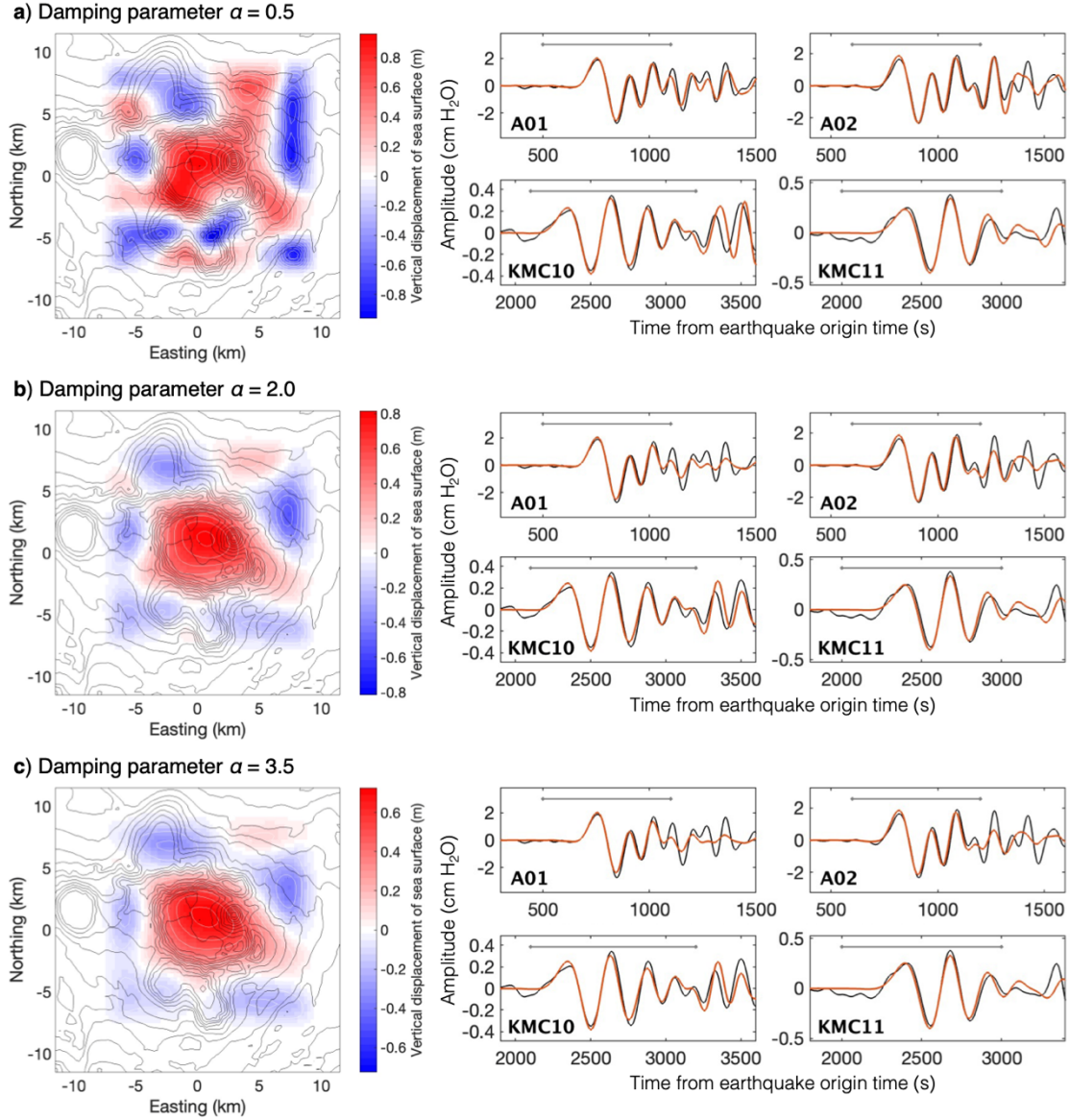
Figure S3. Results of the tsunami waveform inversion for the initial sea-surface displacement with different damping parameters α of (**a**) 0.5, (**b**) 2.0, and (**c**) 3.5 (see Section 3). (Left panel) Red and blue colors represent uplift and subsidence, respectively. Bathymetric contours at 100 m intervals. (Right panels) Comparison of the observed (black) and synthetic (red) tsunami waveforms at representative ocean bottom pressure gauges. By taking a balance between the waveform fit and the smoothness of the displacement, we determine α = 2.0 in this study.
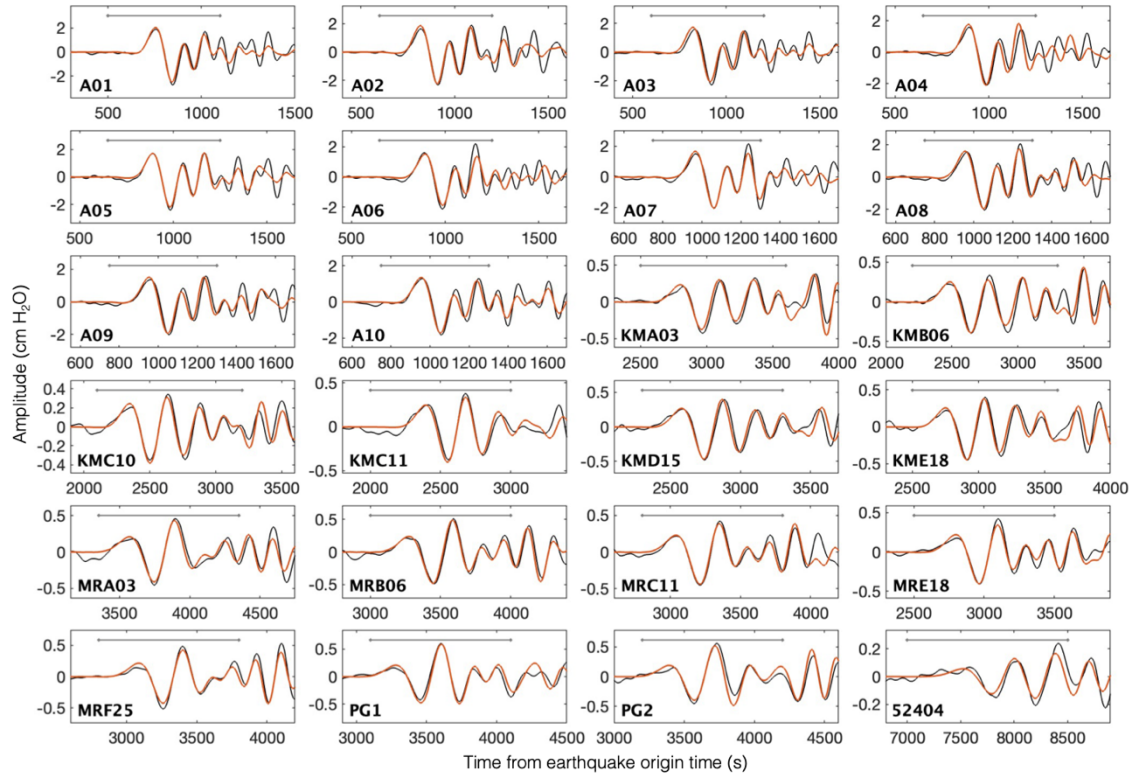
Figure S4. Comparison of the observed (black) and synthetic (red) tsunami waveforms at the ocean bottom pressure gauges from the initial sea-surface displacement model with uplift and subsidence (Figure 2a). The gray line represents the time interval used for the inversion.

a) Source structure

Opening or closure of *the horizontal crack*

Reverse slip along *the ring fault*

b) 2/3-ring arc length

c) Full-ring arc length

d) 1/3-ring arc length

Figure S5. (**a**) Example of the source structure assumed in this study. (**b**–**d**) Three cases of the ring-fault arc length assumed in the source modeling: (**b**) 2/3-ring, (**c**) full-ring, and (**d**) 1/3-ring arc lengths.
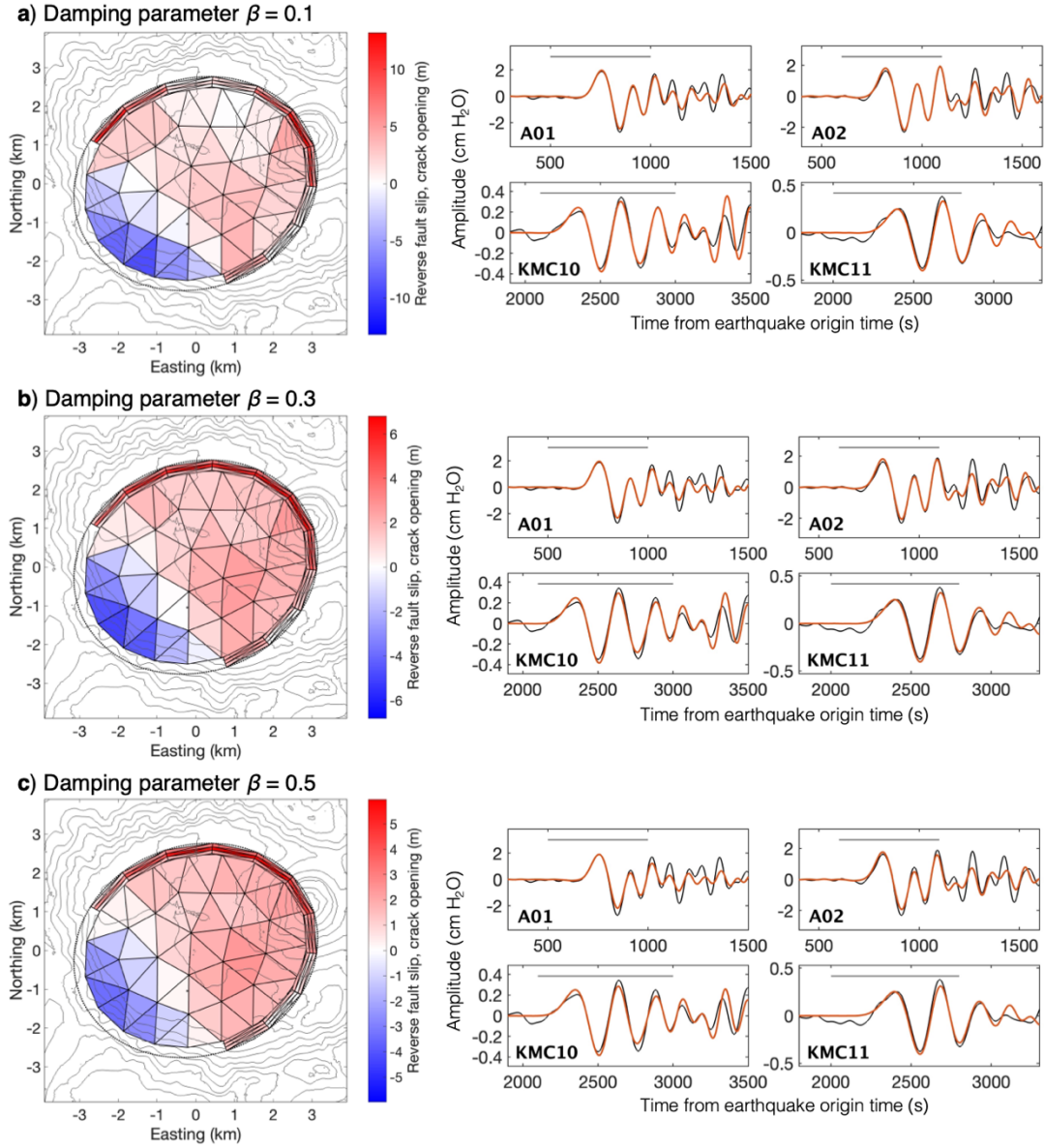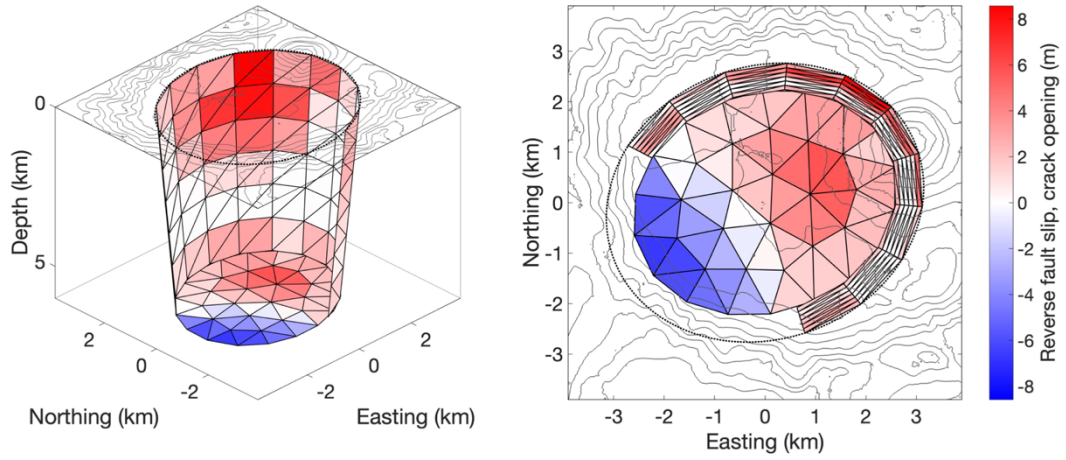
Figure S6. Results of the tsunami waveform inversion for the trapdoor faulting with different damping parameters β of (**a**) 0.1, (**b**) 0.3, and (**c**) 0.5 (see Section 4.2). (Left panel) The red color on the ring fault represents reverse slip. Red and blue colors on the horizontal crack represent vertical opening and closure, respectively. (Right panels) Comparison of the observed (black) and synthetic (red) tsunami waveforms from the model at the ocean bottom pressure gauges. By taking a balance between the waveform fit and the smoothness of the motion, we determine β = 0.3 in this study.
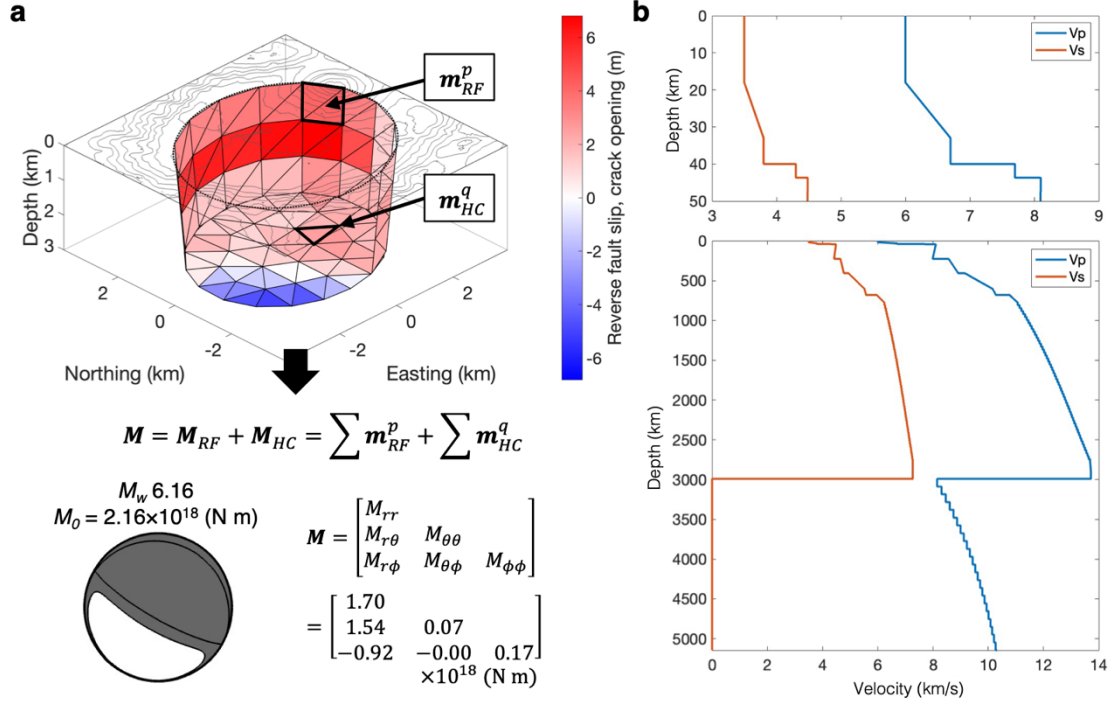
Figure S7. Moment tensor computation and 1-D velocity structure. (**a**) Moment tensor computation process. As an example, the case of the best-fit source model is shown (Figure 3b). (**b**) 1-D velocity structure used in this study (bottom panel). In the top panel, the velocities down to a depth of 50 km are enlarged.

Parameters: (Crack depth , Arc length, Dip angle) = (6.0 km, 2/3-ring, 85°)

Figure S8. Source model inverted from the tsunami waveform inversion, in which we assume a horizontal crack at a depth of 6 km. Color coding is the same as for Figure 3b. We consider this model to be unrealistic (see the text for explanation).

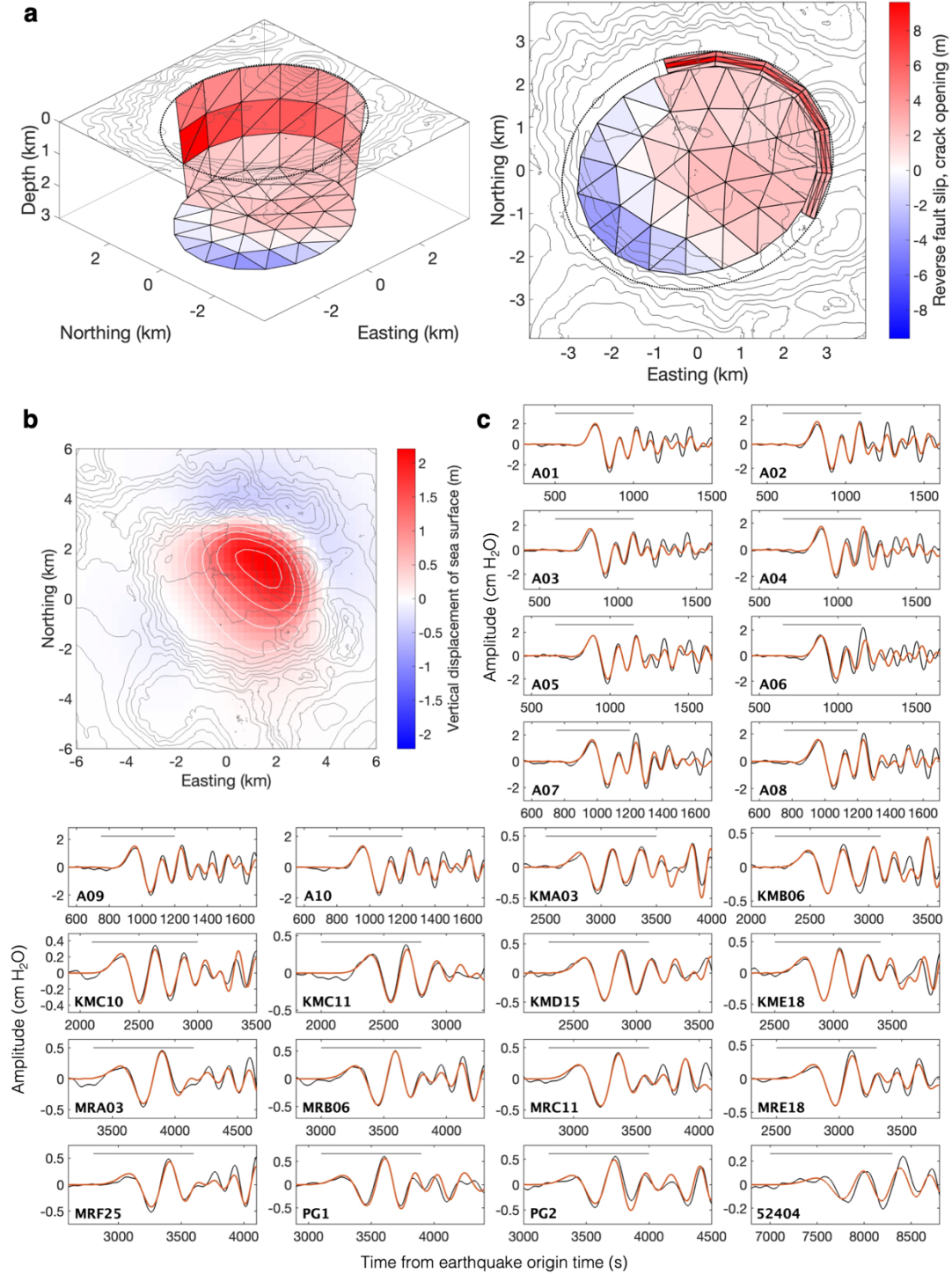Parameters: (Crack depth , Arc length, Dip angle) = (3.0 km, Full-ring, 85.5°)
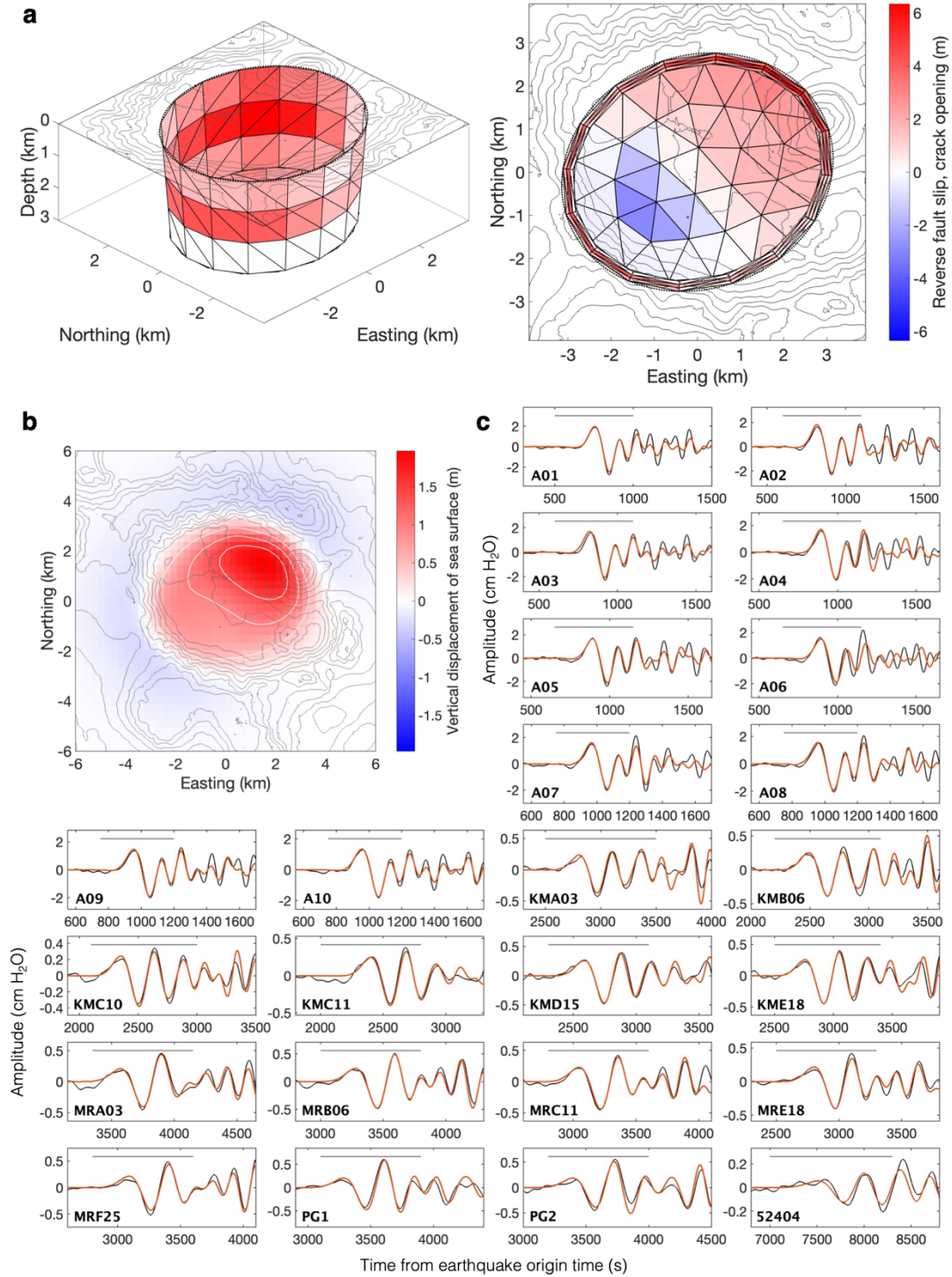
Figure S9. Source modeling results when we assume the source parameters: (Crack depth, Arc length, Dip angle) = (3.0 km, full-ring, 85.5°). (**a**) Source model. See the caption of Figure 3b. (**b**) Vertical displacement of sea surface and (**c**) the tsunami waveforms expected from the model. See the captions of Figure 5.
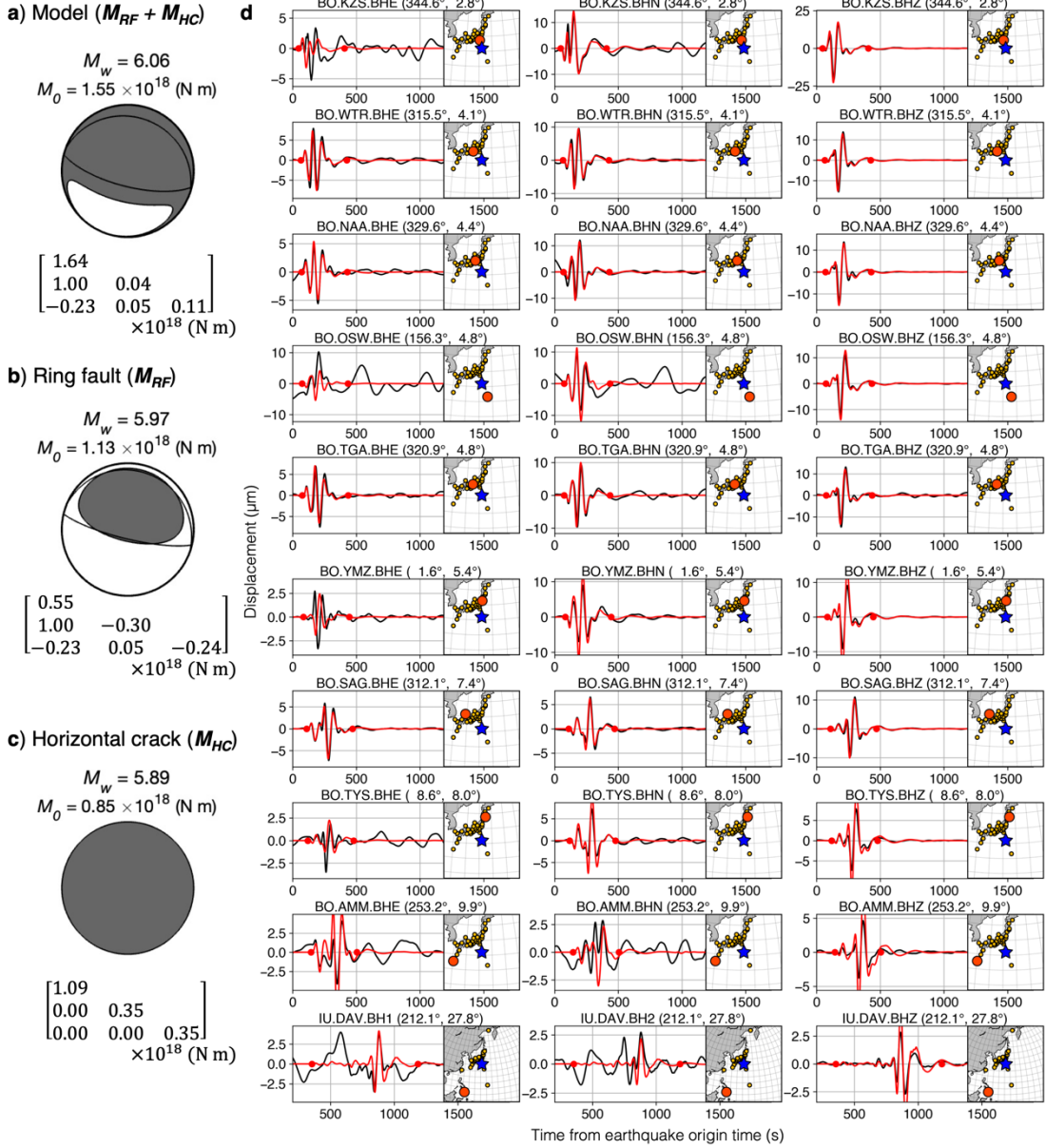
Parameters: (Crack depth , Arc length, Dip angle) = (3.0 km, 1/3-ring, 83.5°)
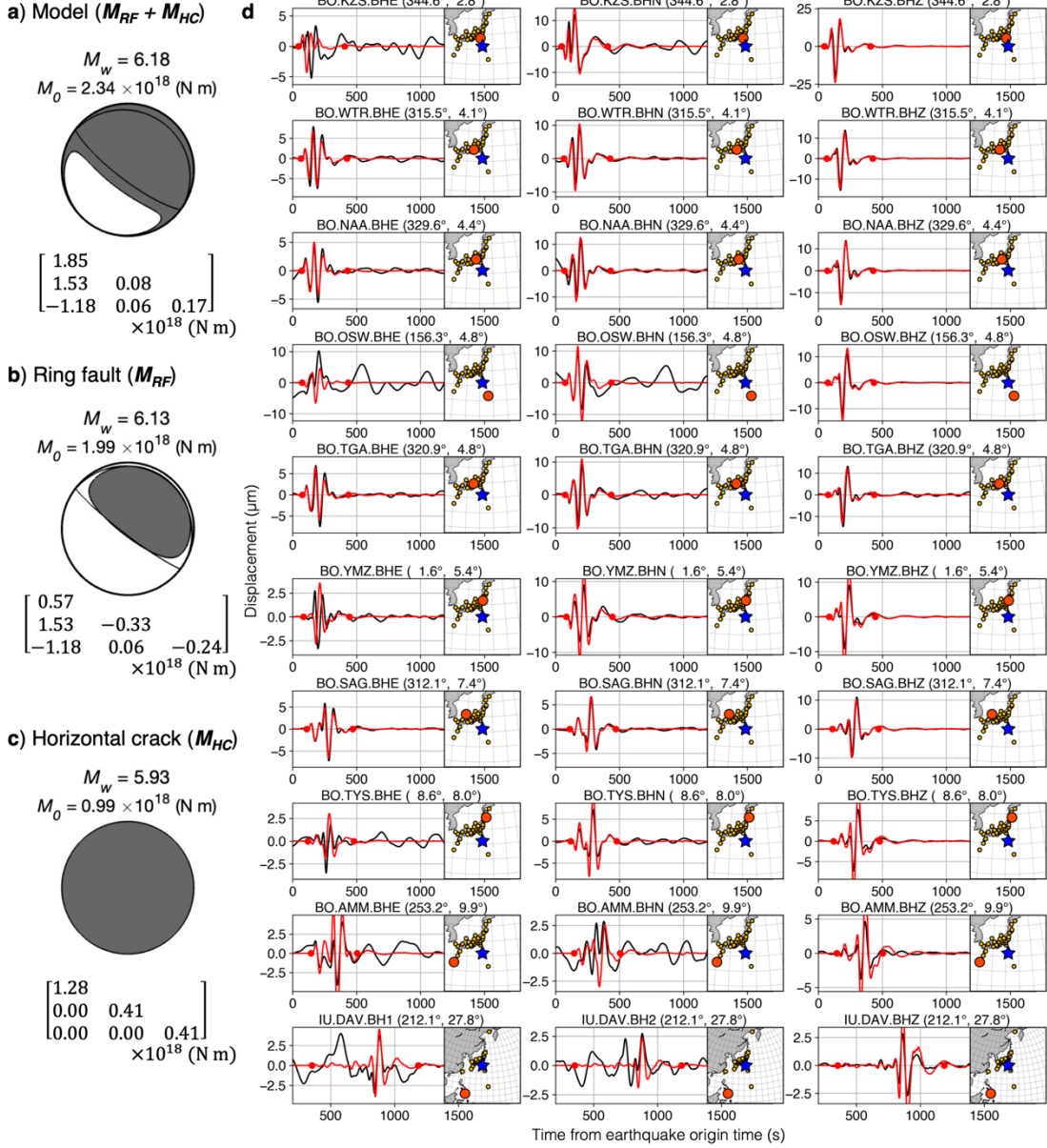

Figure S10. Same as Figure S9, but for those when we assume the source parameters: (Crack depth, Arc length, Dip angle) = (3.0 km, 1/3-ring, 83.5°).

Parameters: (Crack depth, Arc length, Dip angle) = (3.0 km, Full-ring, 85.5°)

a) Model ($M_{RF} + M_{HC}$)

$M_w = 6.06$
$M_0 = 1.55 \times 10^{18}$ (N m)

$$\begin{bmatrix} 1.64 & & \\ 1.00 & 0.04 & \\ -0.23 & 0.05 & 0.11 \end{bmatrix}$$
$\times 10^{18}$ (N m)

b) Ring fault (M_{RF})

$M_w = 5.97$
$M_0 = 1.13 \times 10^{18}$ (N m)

$$\begin{bmatrix} 0.55 & & \\ 1.00 & -0.30 & \\ -0.23 & 0.05 & -0.24 \end{bmatrix}$$
$\times 10^{18}$ (N m)

c) Horizontal crack (M_{HC})

$M_w = 5.89$
$M_0 = 0.85 \times 10^{18}$ (N m)

$$\begin{bmatrix} 1.09 & & \\ 0.00 & 0.35 & \\ 0.00 & 0.00 & 0.35 \end{bmatrix}$$
$\times 10^{18}$ (N m)

d

Figure S11. Same as Figure 7, but for the full-ring arc-length model shown in Figure S9. In **d**, black and red lines represent the observed (black) and synthetic (red) seismograms (period = 60–250 s) at representative stations, computed with the moment tensor shown in **a**. See the caption of Figure 7.

14

Parameters: (Crack depth, Arc length, Dip angle) = (3.0 km, 1/3-ring, 83.5°)

a) Model ($M_{RF} + M_{HC}$)

$M_w = 6.18$
$M_0 = 2.34 \times 10^{18}$ (N m)

$$\begin{bmatrix} 1.85 & & \\ 1.53 & 0.08 & \\ -1.18 & 0.06 & 0.17 \end{bmatrix}$$
$\times 10^{18}$ (N m)

b) Ring fault (M_{RF})

$M_w = 6.13$
$M_0 = 1.99 \times 10^{18}$ (N m)

$$\begin{bmatrix} 0.57 & & \\ 1.53 & -0.33 & \\ -1.18 & 0.06 & -0.24 \end{bmatrix}$$
$\times 10^{18}$ (N m)

c) Horizontal crack (M_{HC})

$M_w = 5.93$
$M_0 = 0.99 \times 10^{18}$ (N m)

$$\begin{bmatrix} 1.28 & & \\ 0.00 & 0.41 & \\ 0.00 & 0.00 & 0.41 \end{bmatrix}$$
$\times 10^{18}$ (N m)

d



Displacement (μm)

Time from earthquake origin time (s)

Figure S12. Same as Figure 7, but for the 1/3-ring arc-length model shown in Figure S10. In **d**, black and red lines represent the observed (black) and synthetic (red) seismograms (period = 60–250 s) at representative stations, computed with the moment tensor shown in **a**. See the caption of Figure 7.

15
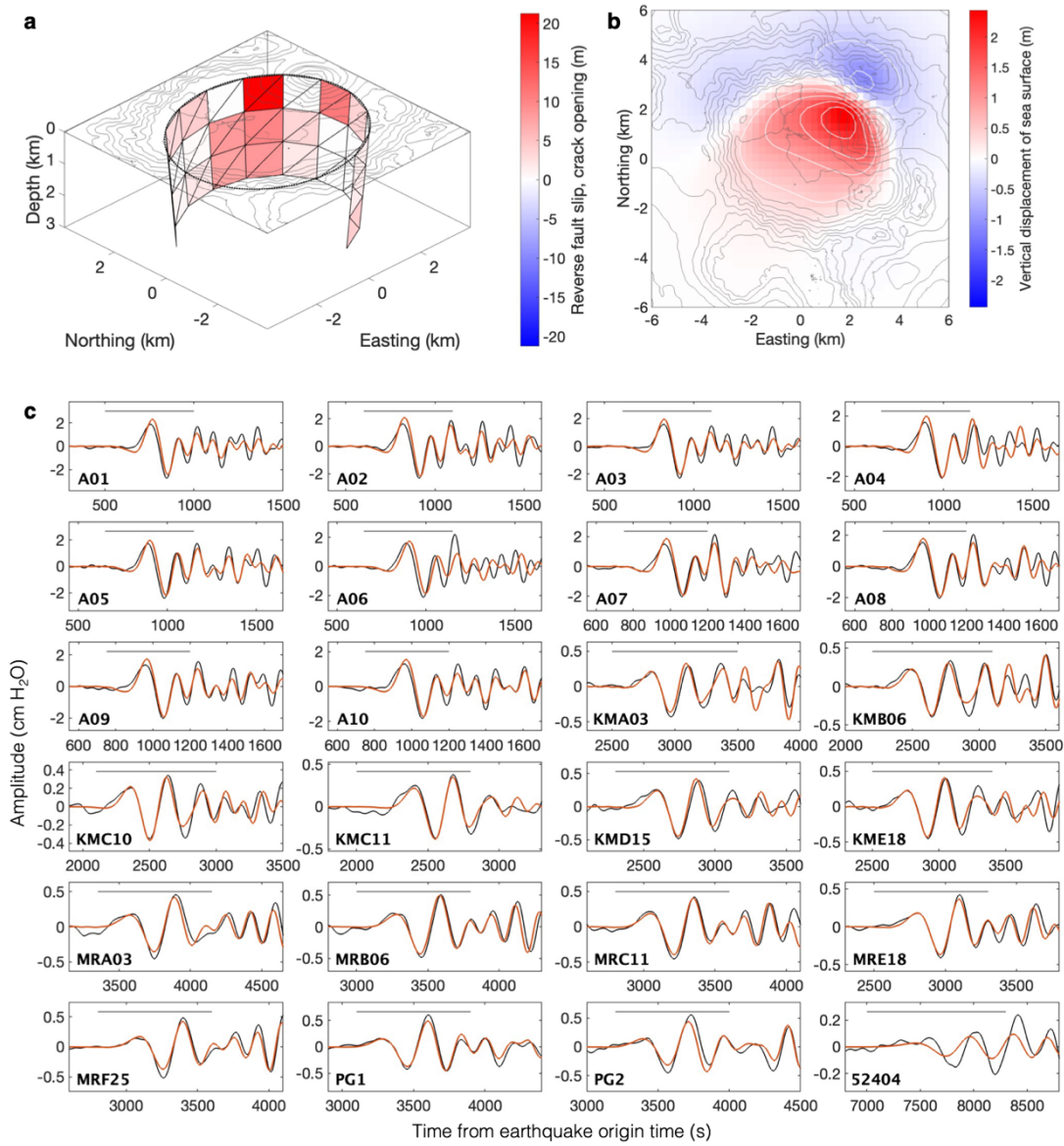
Figure S13. Source model inverted from the tsunami waveform inversion, in which we assume only the ring fault. See the caption of Figure 4. Note that with only the ring fault, the waveform fit is overall worse, compared to the tsunami waveforms from the trapdoor faulting model (Figure 5).
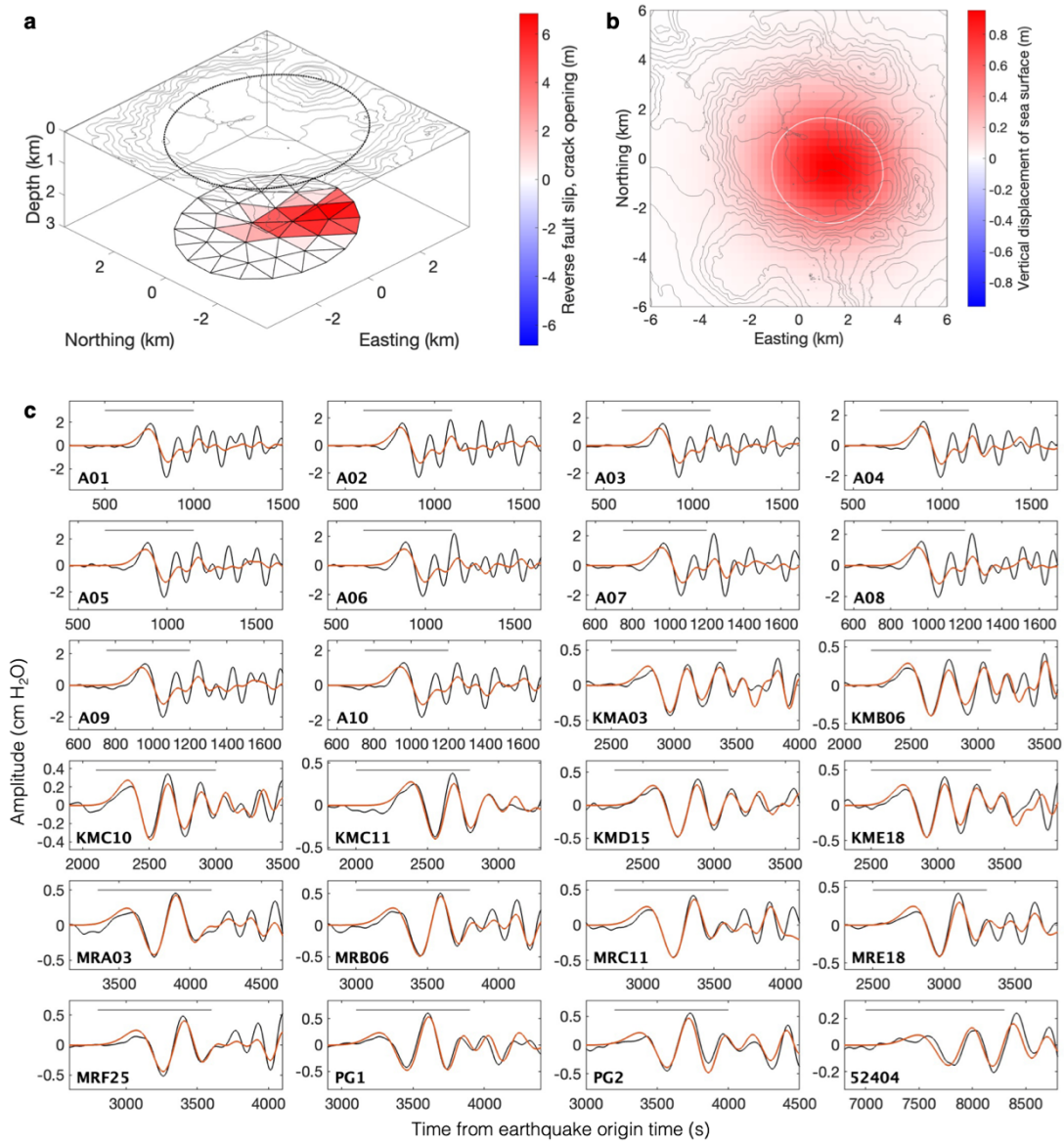
Figure S14. Source model inverted from the tsunami waveform inversion, in which we assume only the horizontal crack. See the caption of Figure 4. Note that with only the horizontal crack, the waveform fit is clearly worse, compared to the tsunami waveforms from the trapdoor faulting model (Figure 5).
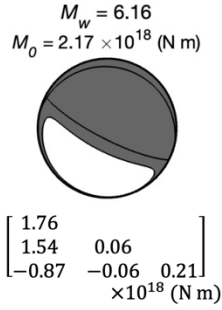
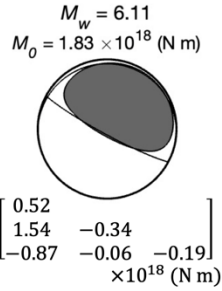Parameters: (Crack depth , Arc length, Dip angle) = (3.0 km, 2/3-ring, 83–87°)
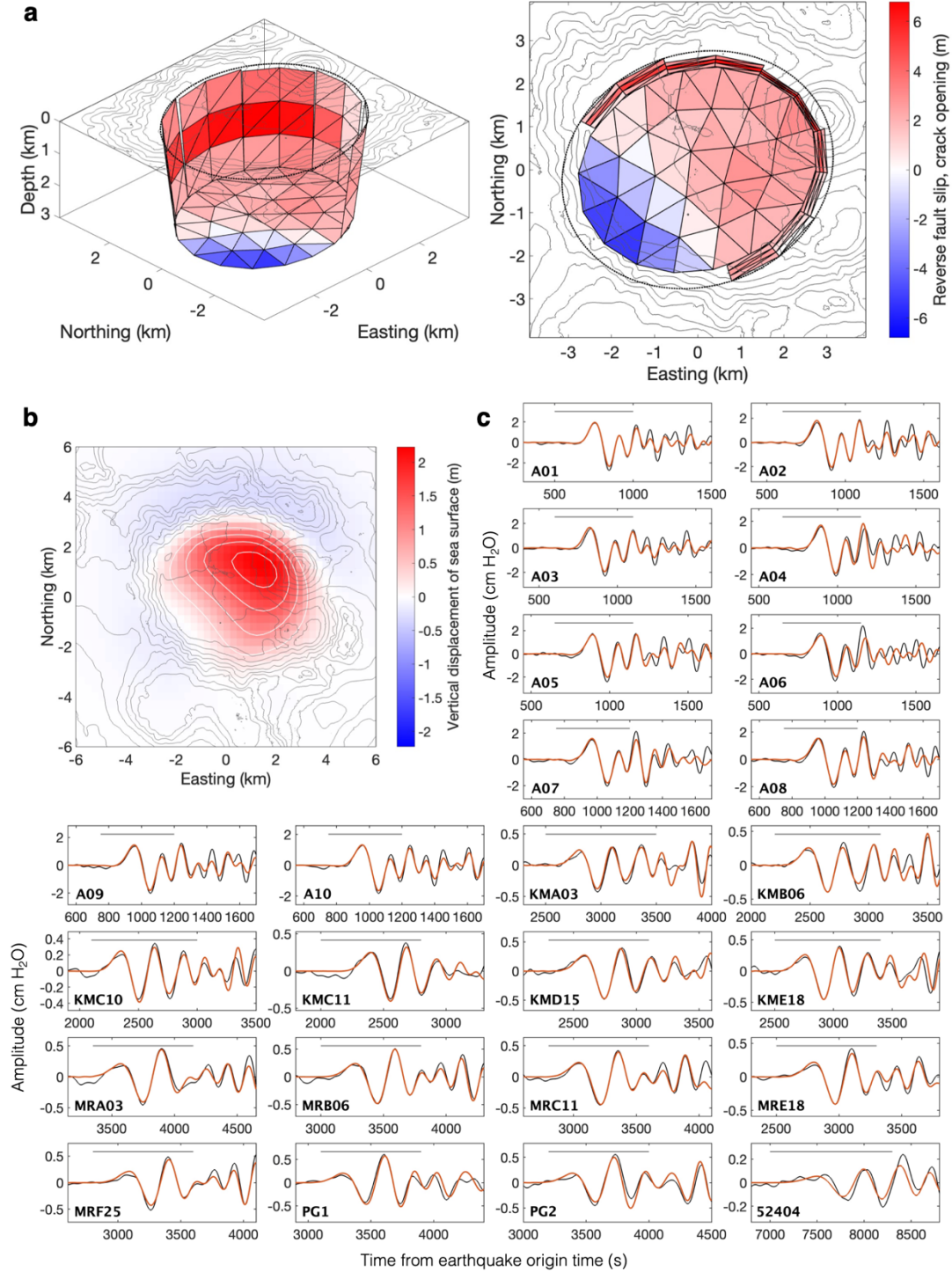
Figure S15. Same as Figure S9, but for those when we assume the source parameters: (Crack depth, Arc length, Dip angle) = (3.0 km, 2/3-ring, 83–87°). Note that the dip angle is not uniform along the ring fault (see Text S3).

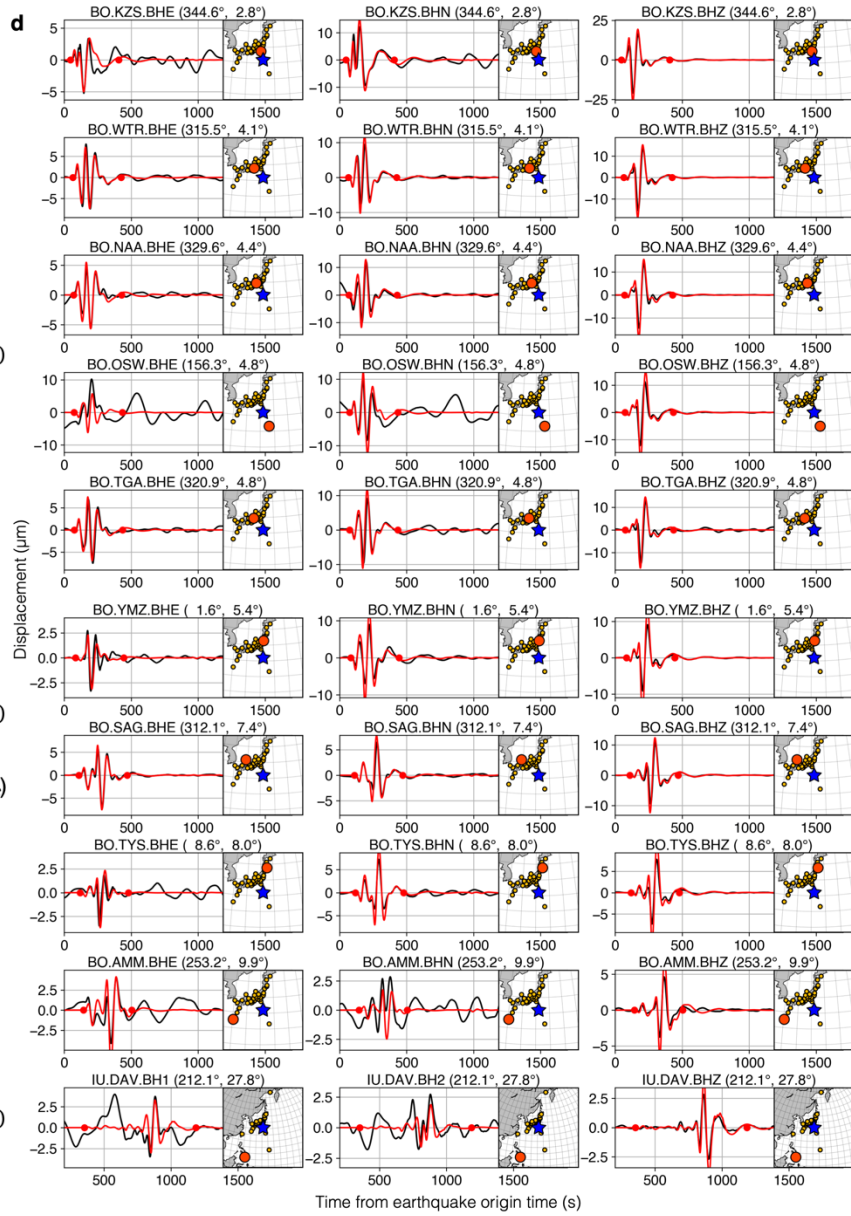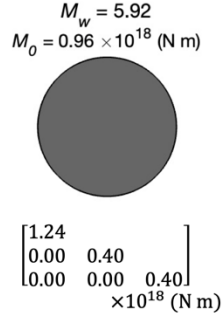Parameters: (Crack depth, Arc length, Dip angle) = (3.0 km, 2/3-ring, 83–87°)

a) Model ($M_{RF} + M_{HC}$)
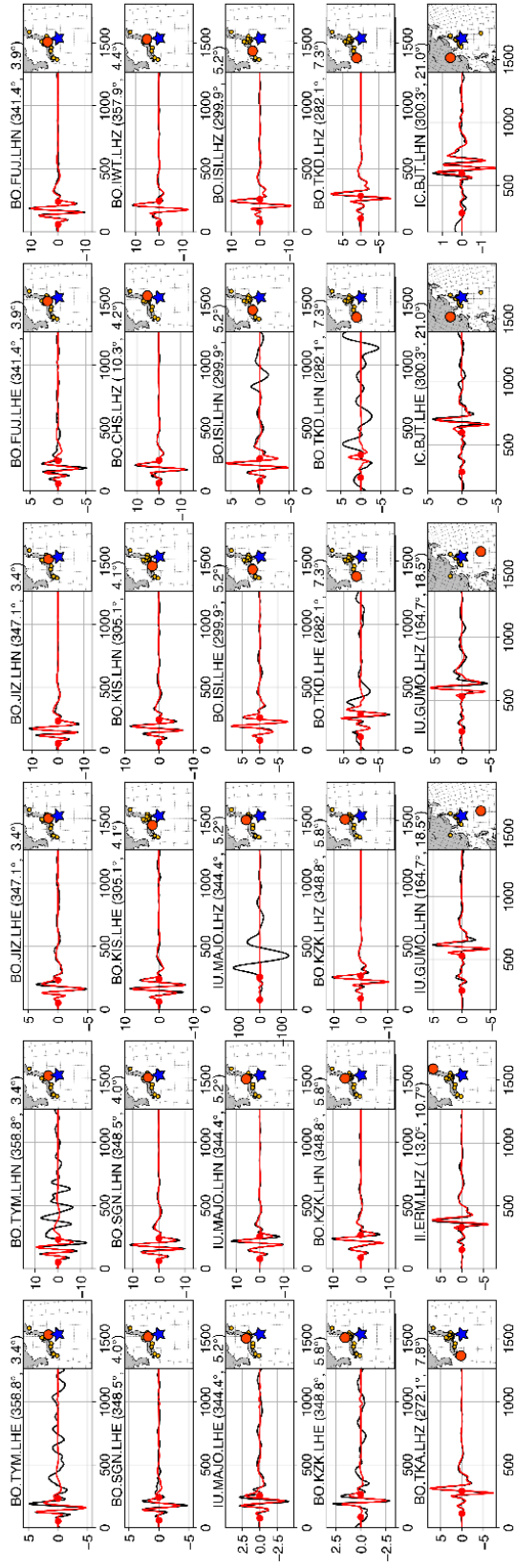
$M_w = 6.16$
$M_0 = 2.17 \times 10^{18}$ (N m)

$$\begin{bmatrix} 1.76 & & \\ 1.54 & 0.06 & \\ -0.87 & -0.06 & 0.21 \end{bmatrix}$$
$\times 10^{18}$ (N m)

b) Ring fault (M_{RF})

$M_w = 6.11$
$M_0 = 1.83 \times 10^{18}$ (N m)

$$\begin{bmatrix} 0.52 & & \\ 1.54 & -0.34 & \\ -0.87 & -0.06 & -0.19 \end{bmatrix}$$
$\times 10^{18}$ (N m)

c) Horizontal crack (M_{HC})

$M_w = 5.92$
$M_0 = 0.96 \times 10^{18}$ (N m)

$$\begin{bmatrix} 1.24 & & \\ 0.00 & 0.40 & \\ 0.00 & 0.00 & 0.40 \end{bmatrix}$$
$\times 10^{18}$ (N m)

d

BO.KZS.BHE (344.6°, 2.8°)   BO.KZS.BHN (344.6°, 2.8°)   BO.KZS.BHZ (344.6°, 2.8°)
BO.WTR.BHE (315.5°, 4.1°)   BO.WTR.BHN (315.5°, 4.1°)   BO.WTR.BHZ (315.5°, 4.1°)
BO.NAA.BHE (329.6°, 4.4°)   BO.NAA.BHN (329.6°, 4.4°)   BO.NAA.BHZ (329.6°, 4.4°)
BO.OSW.BHE (156.3°, 4.8°)   BO.OSW.BHN (156.3°, 4.8°)   BO.OSW.BHZ (156.3°, 4.8°)
BO.TGA.BHE (320.9°, 4.8°)   BO.TGA.BHN (320.9°, 4.8°)   BO.TGA.BHZ (320.9°, 4.8°)
BO.YMZ.BHE (1.6°, 5.4°)   BO.YMZ.BHN (1.6°, 5.4°)   BO.YMZ.BHZ (1.6°, 5.4°)
BO.SAG.BHE (312.1°, 7.4°)   BO.SAG.BHN (312.1°, 7.4°)   BO.SAG.BHZ (312.1°, 7.4°)
BO.TYS.BHE (8.6°, 8.0°)   BO.TYS.BHN (8.6°, 8.0°)   BO.TYS.BHZ (8.6°, 8.0°)
BO.AMM.BHE (253.2°, 9.9°)   BO.AMM.BHN (253.2°, 9.9°)   BO.AMM.BHZ (253.2°, 9.9°)
IU.DAV.BH1 (212.1°, 27.8°)   IU.DAV.BH2 (212.1°, 27.8°)   IU.DAV.BHZ (212.1°, 27.8°)

Displacement (μm)

Time from earthquake origin time (s)

**Figure S16.** Same as Figure 7, but for the 1/3-ring arc-length model shown in Figure S15.

19

Figure S17. Model performance of the MT inversion for the 1996 earthquake. The vertical and horizontal axes represent displacement (in the [μm] scale) and time from the earthquake origin time (in the [s] scale). Red and black lines represent synthetic and observed waveforms, respectively. The time window for the inversion is indicated by red dots.
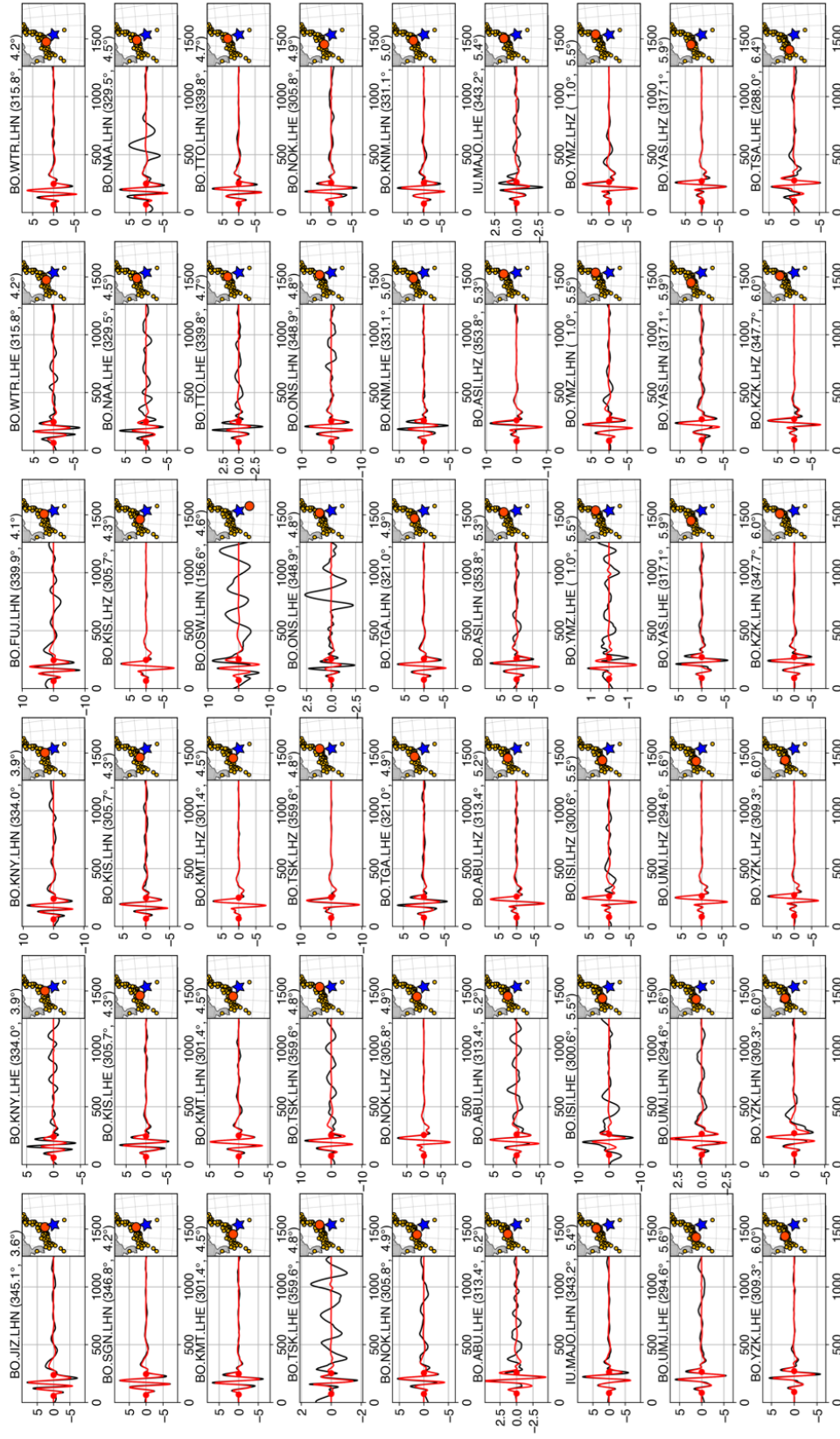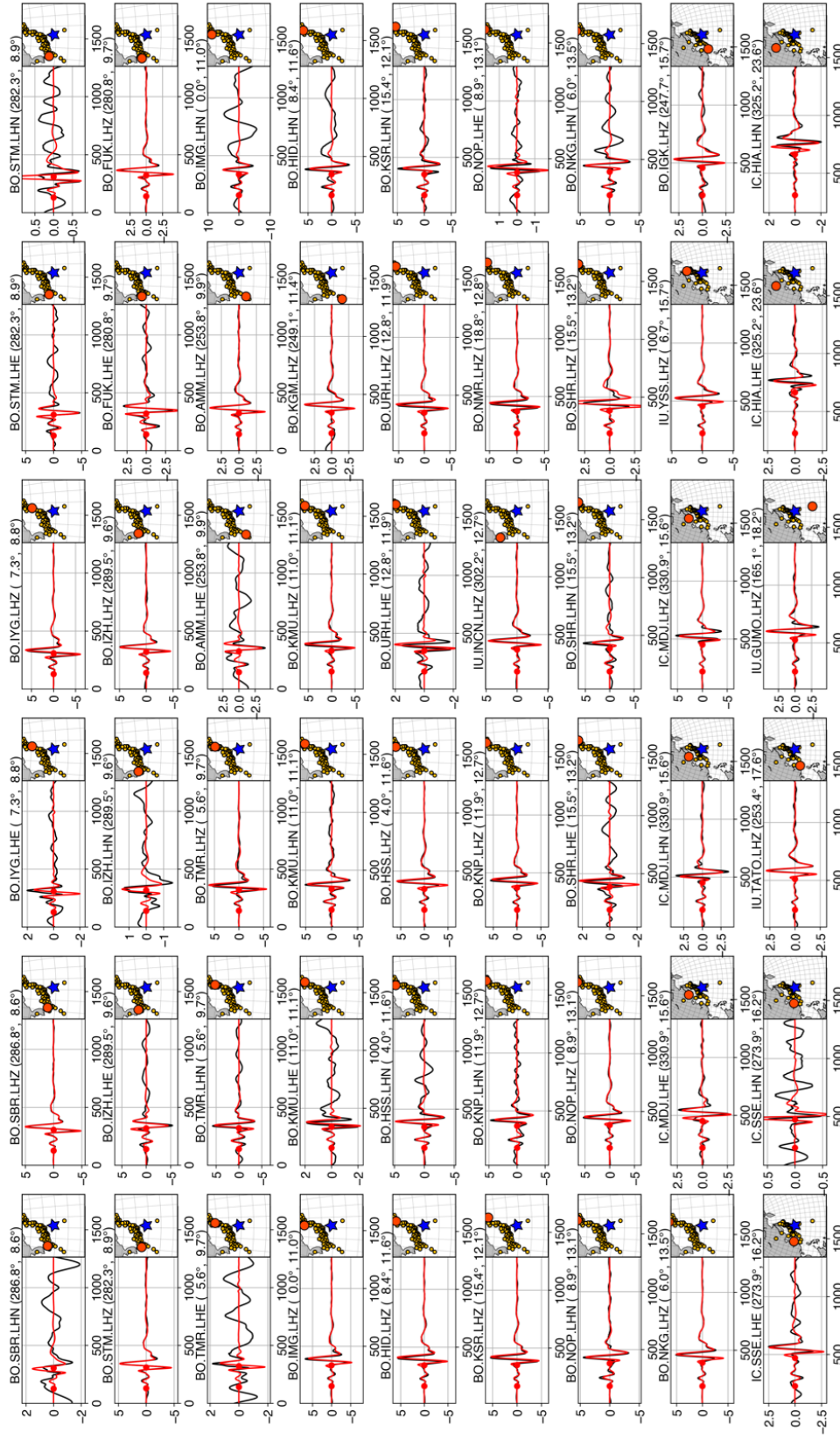
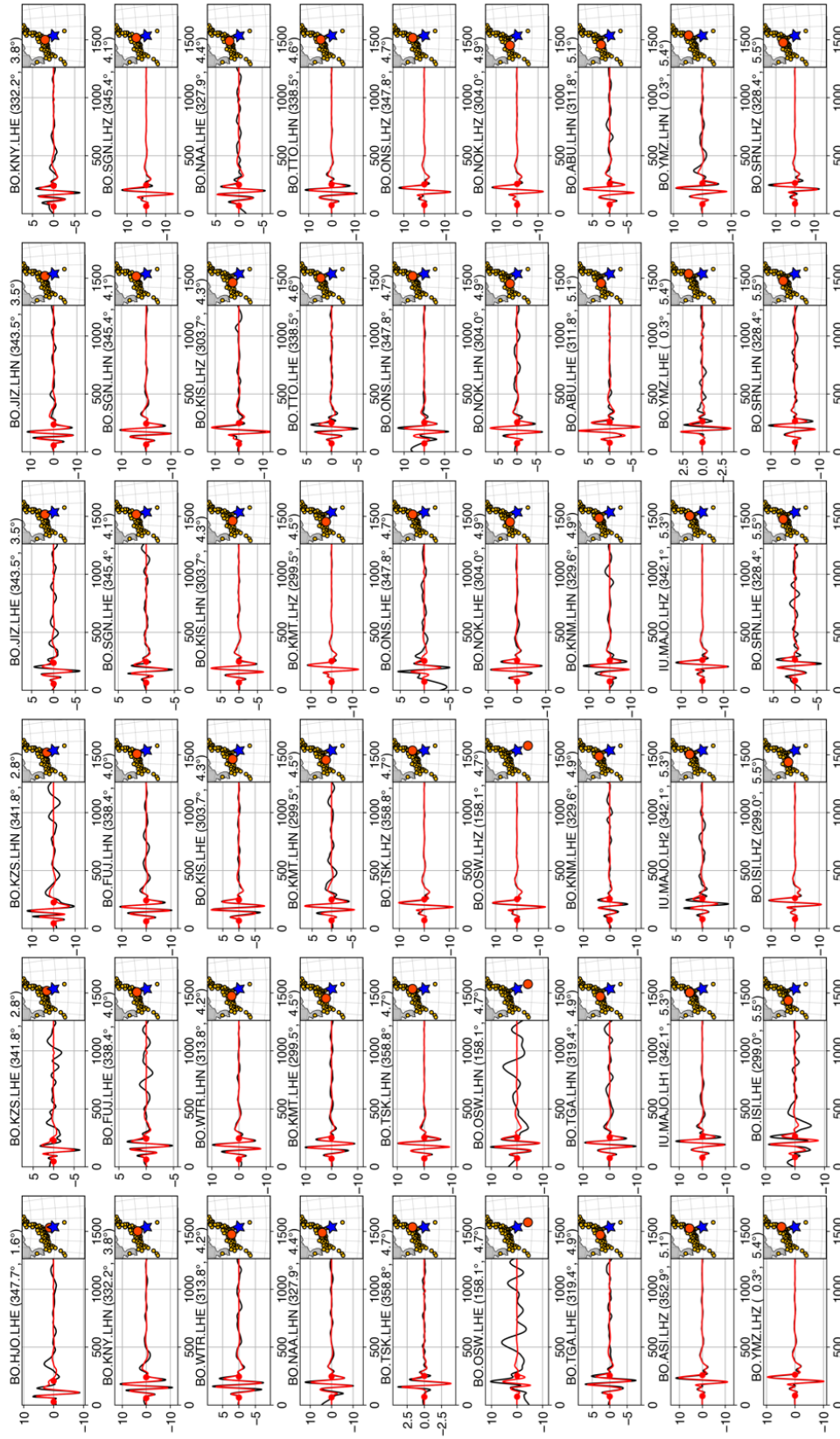**Figure S18**. Model performance of the MT inversion for the 2006 earthquake.
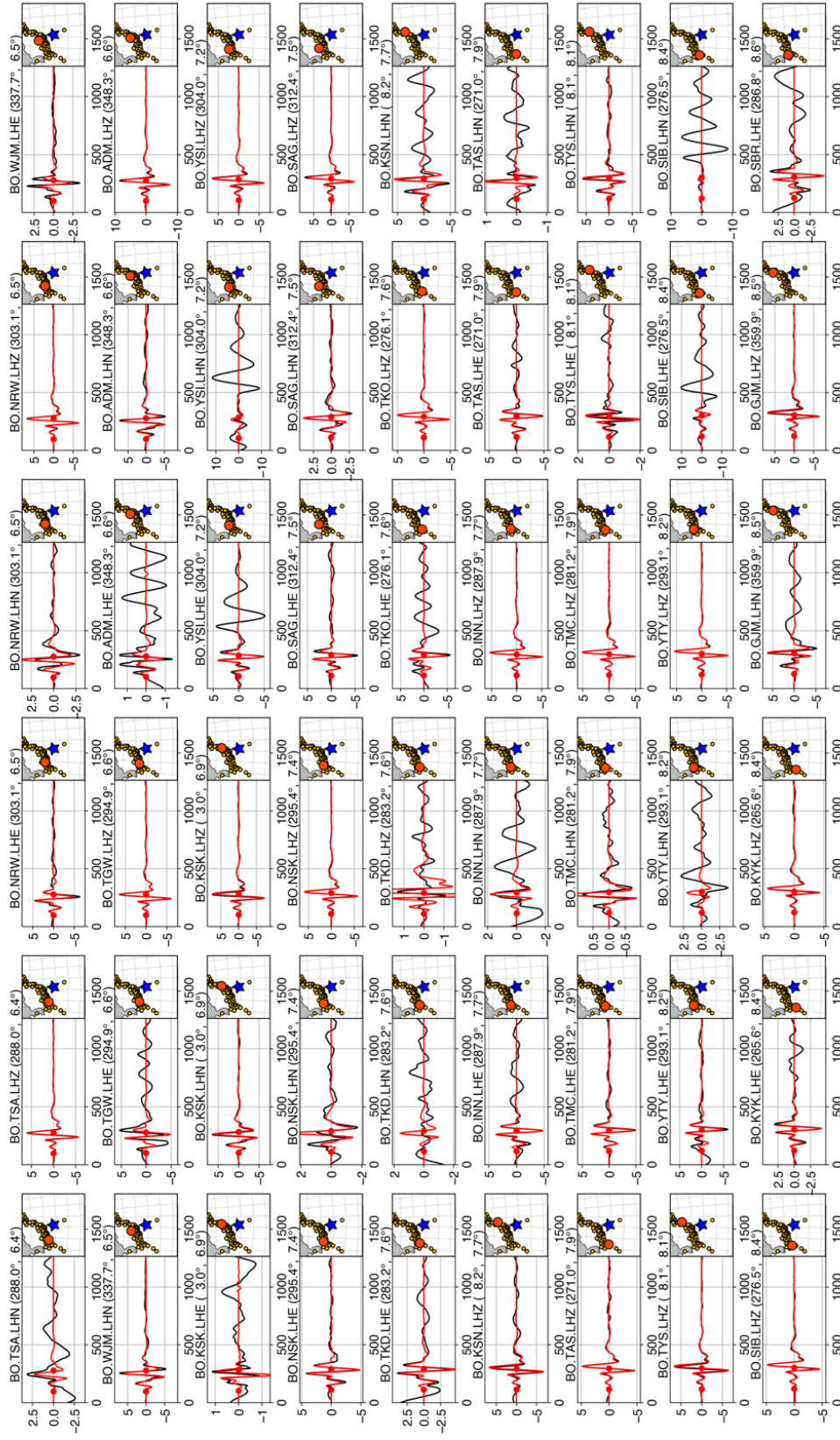
Figure S18. Model performance of the MT inversion for the 2006 earthquake (continued).

22

Figure S18. Model performance of the MT inversion for the 2006 earthquake (continued).

23

Figure S19. Model performance of the MT inversion for the 2015 earthquake.
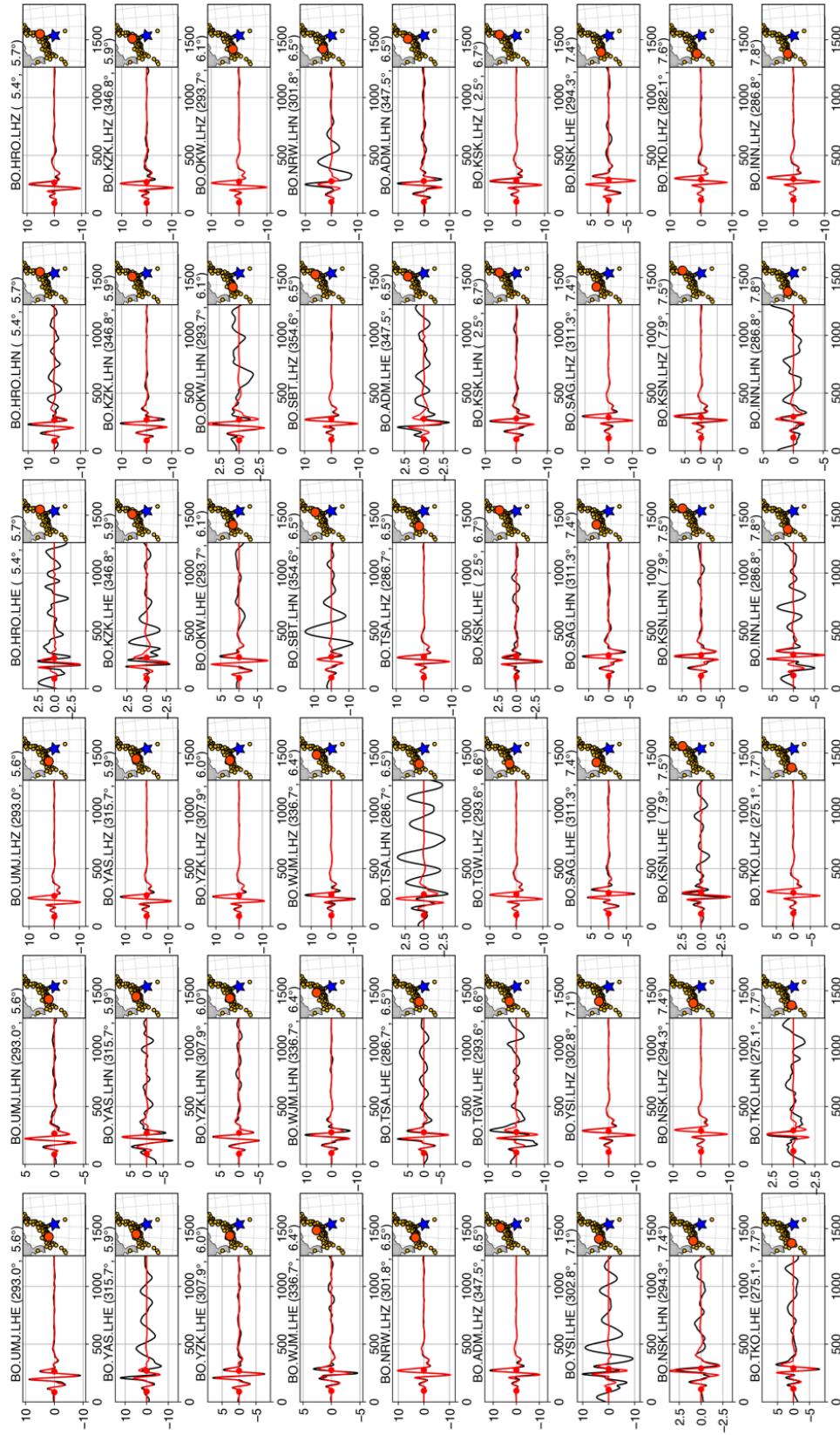
Figure S19. Model performance of the MT inversion for the 2015 earthquake (continued).

Figure S19. Model performance of the MT inversion for the 2015 earthquake (continued).
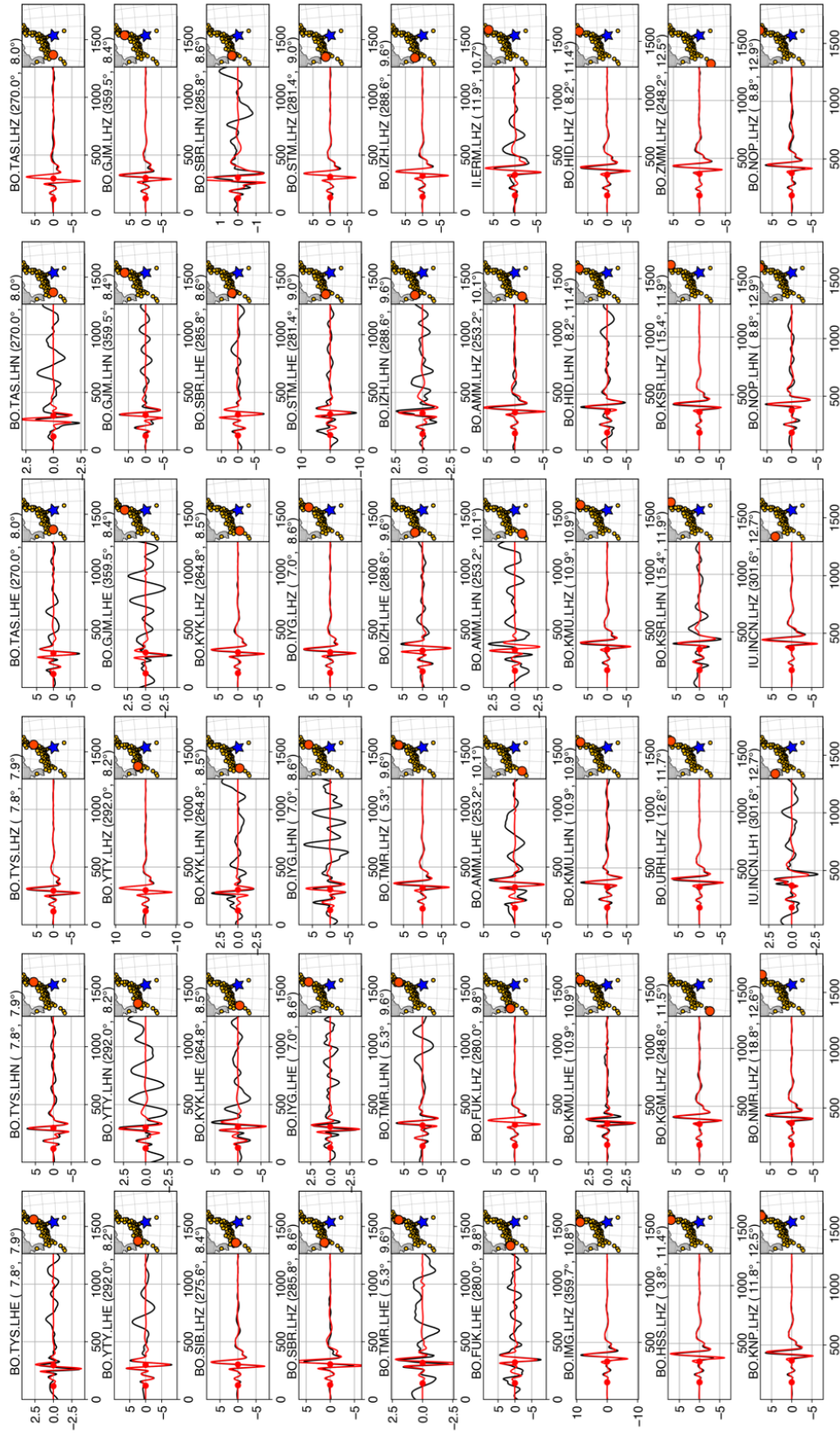
Figure S19. Model performance of the MT inversion for the 2015 earthquake (continued).
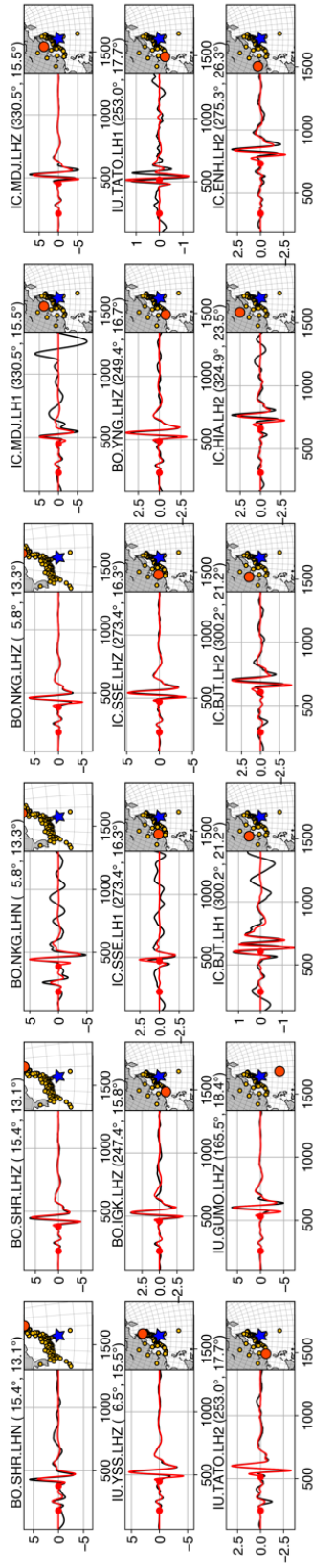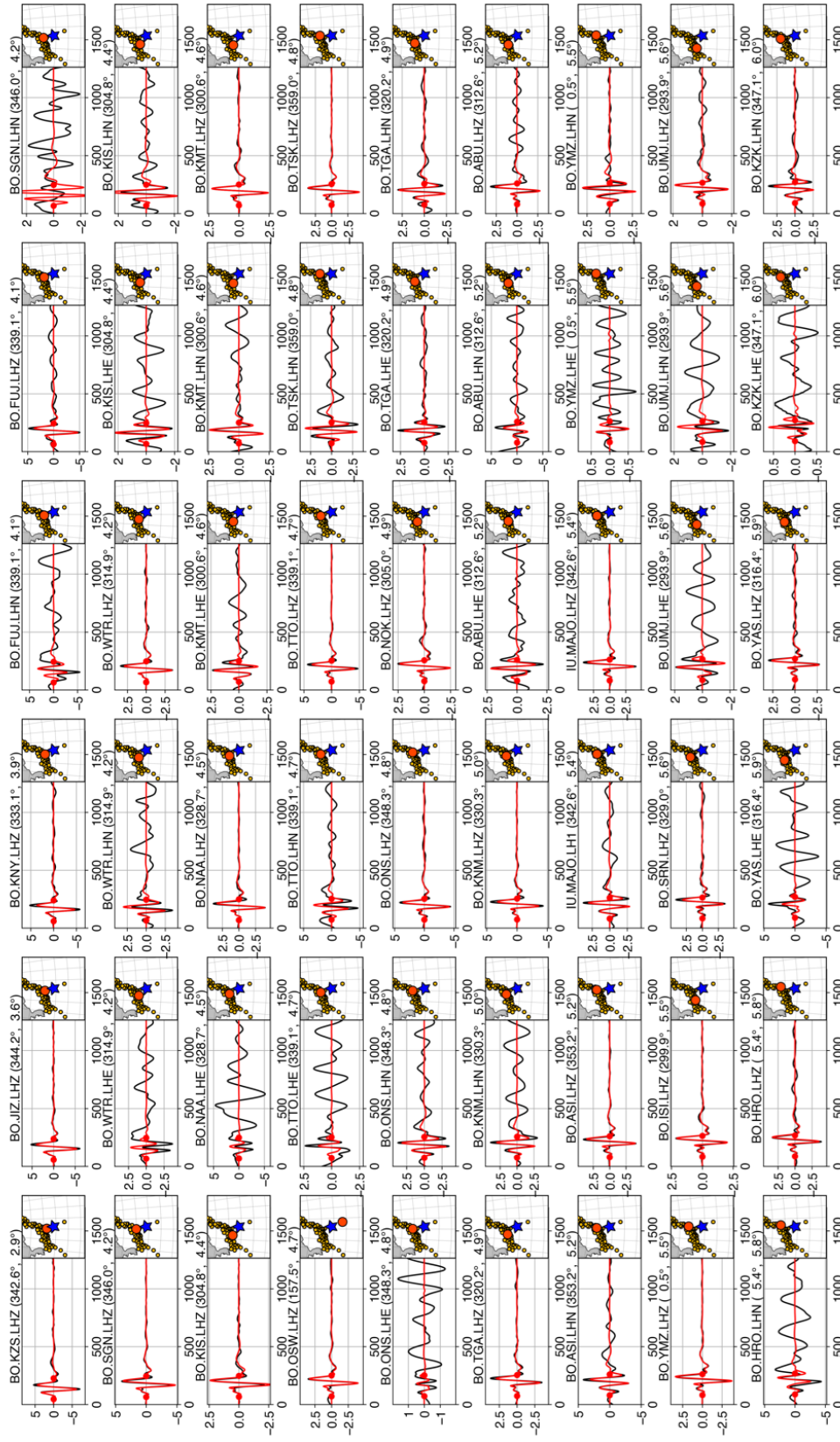
Figure S20. Model performance of the MT inversion for the 2018 earthquake.
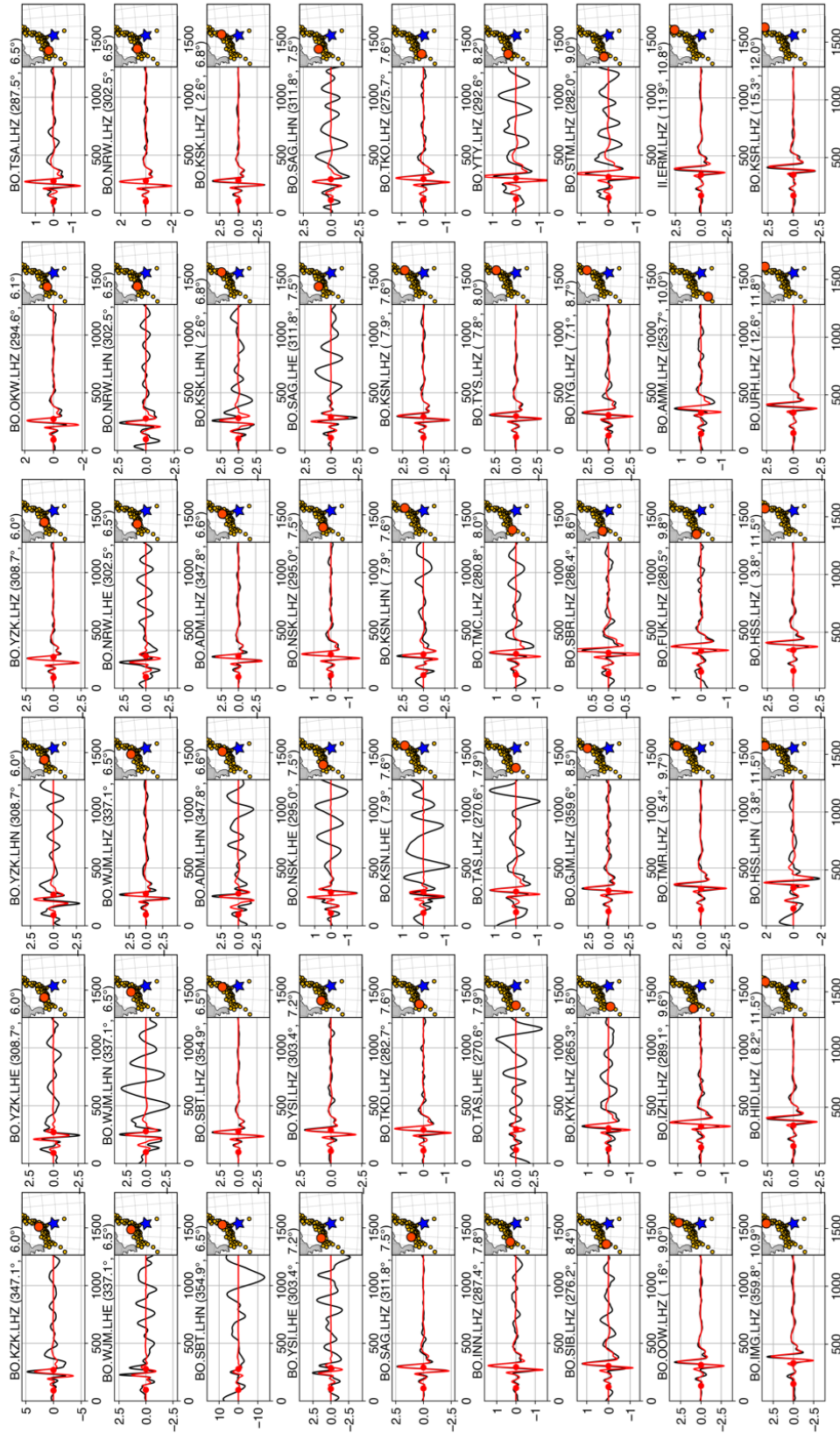
Figure S20. Model performance of the MT inversion for the 2018 earthquake (continued).

29
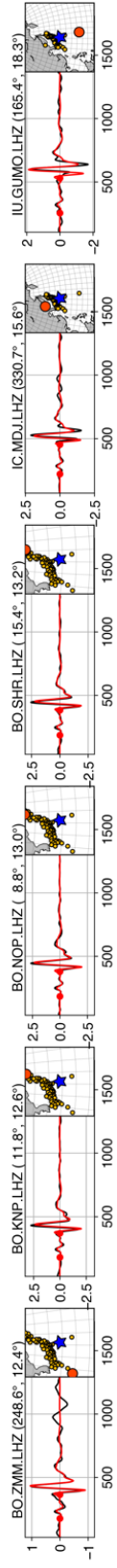
Figure S20. Model performance of the MT inversion for the 2018 earthquake (continued).

Parameters: (Crack depth, Arc length, Dip angle) = (3.0 km, 2/3-ring, 77°)
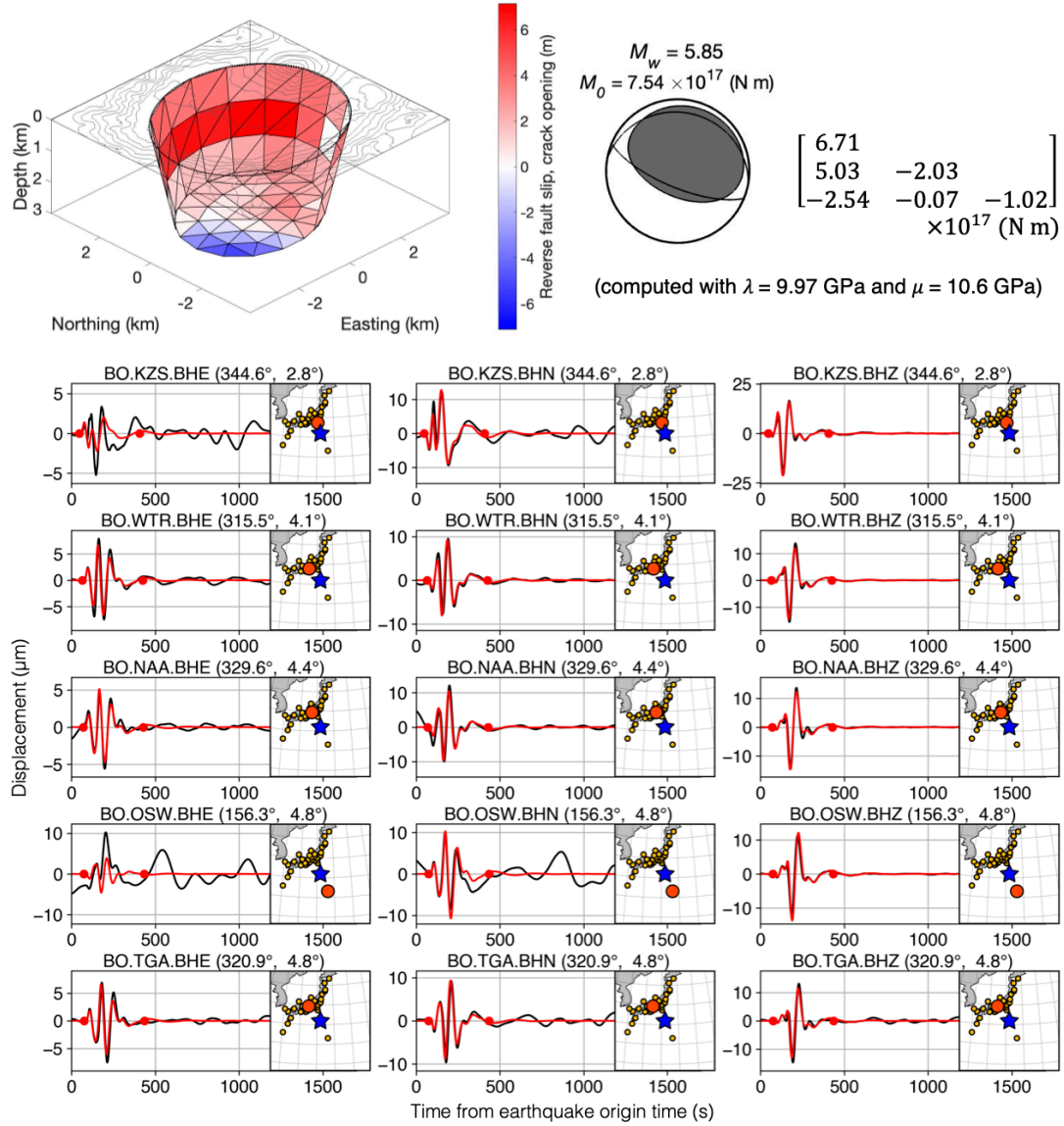
Figure S21. Synthetic long-period seismic waveforms when we assume low rigidity (λ = 9.97 GPa and μ = 10.6 GPa) for the moment tensor computation. This shows the model with a 2/3-ring fault with a dip angle of 77°.

Table S1. Earthquake information of volcanic earthquakes at Sumisu caldera, reported by the GCMT catalog (Ekström, Nettles, and Dziewoński 2012). Note that shallow source depths cannot be determined accurately with long-period seismic data used for the catalogue.

Event	Date (Y/M/D)	Time (h:m:s)	Longitude	Latitudes	Depth (km)	M_W	M_S
1	1984/6/13	2:29:29	139.93°	31.39°	15.2	5.6	5.4
2	1996/9/4	18:16:07	140.06°	31.48°	24.4	5.7	5.1
3	2006/1/1	7:12:07	140.07°	31.51°	12	5.6	5.0
4	2015/5/2	16:50:50	139.94°	31.47°	12	5.7	5.7
5	2018/5/6	6:04:06	139.98°	31.51°	12	5.4	5.4

Table S2. Stations used for the computation of the long-period seismic waves. Station list of broad-band seismic stations used for the forward simulation of long-period seismic waves. For each station, we use the record of the three components.

Network	Station code	Distance (degree)	Azimuth (degree)
F-net	KZS	2.82	344.57
F-net	JIZ	3.54	345.74
F-net	KNY	3.77	334.25
F-net	WTR	4.11	315.49
F-net	SGN	4.12	347.31
F-net	KIS	4.24	305.17
F-net	NAA	4.36	329.6
F-net	KMT	4.43	300.79
F-net	TTO	4.63	340.16
F-net	TSK	4.72	0.36
F-net	OSW	4.75	156.29
F-net	NOK	4.78	305.26
F-net	TGA	4.82	320.88
F-net	KNM	4.85	331.16
GSN	MAJO	5.28	343.59
F-net	YMZ	5.43	1.62
F-net	UMJ	5.49	293.93
F-net	SRN	5.5	329.74
F-net	YZK	5.9	309
F-net	WJM	6.41	337.87
F-net	KSK	6.77	3.54
F-net	NSK	7.34	294.95
F-net	SAG	7.36	312.11
F-net	TKO	7.53	275.4
F-net	KSN	7.57	8.77
F-net	TYS	7.97	8.64
F-net	KYK	8.36	264.9
F-net	SBR	8.52	286.26
F-net	IZH	9.5	289.03
F-net	TMR	9.66	6
F-net	AMM	9.91	253.18
F-net	KMU	10.98	11.41
GSN	TATO	17.58	252.97
GSN	GUMO	18.35	164.98
GSN	DAV	27.8	212.13
GSN	MA2	29	11.26

Table S3. Results of the moment tensor analysis. Moment magnitudes, scalar seismic moments, moment tensors, and half durations of the repeating earthquakes. Note that $M_{r\theta}$ and $M_{r\phi}$ determined from long-period seismic waveforms are unreliable due to shallow source depths (Sandanbata et al. 2021).

Event	M_w	M_0 (x 10^{18} N m)	Moment tensor (x 10^{18} N m)						Half duration (s)
			M_{rr}	$M_{\theta\theta}$	$M_{\phi\phi}$	$M_{r\theta}$	$M_{r\phi}$	$M_{\theta\phi}$	
1996	5.99	1.20	0.384	-0.221	-0.164	0.282	-1.140	-0.069	5.3
2006	5.88	0.82	0.286	-0.189	-0.097	-0.159	-0.780	-0.024	8.0
2015	6.01	1.30	0.385	-0.225	-0.160	-0.311	-1.226	-0.071	5.0
2018	5.58	0.28	0.103	-0.091	-0.011	-0.107	-0.252	-0.006	4.0

Data Set S1. Source models of the trapdoor faulting (separate file). This dataset includes four source models presented in Figures 3b, S10a, S11a, and S15a.

Supplementary References

Duputel, Z., Rivera, L., Kanamori, H., & Hayes, G. (2012). W phase source inversion for moderate to large earthquakes (1990–2010). *Geophysical Journal International*, *189*(2), 1125–1147. https://doi.org/10.1111/j.1365-246X.2012.05419.x

Ekström, G., Nettles, M., & Dziewoński, A. M. (2012). The global CMT project 2004–2010: Centroid-moment tensors for 13,017 earthquakes. *Physics of the Earth and Planetary Interiors*, *200-201*, 1–9. https://doi.org/10.1016/j.pepi.2012.04.002

Hayes, G. P., Rivera, L., & Kanamori, H. (2009). Source Inversion of the W-Phase: Real-time Implementation and Extension to Low Magnitudes. *Seismological Research Letters*, *80*(5), 817–822. https://doi.org/10.1785/gssrl.80.5.817

Kanamori, H., & Rivera, L. (2008). Source inversion of Wphase: speeding up seismic tsunami warning. *Geophysical Journal International*, *175*(1), 222–238. https://doi.org/10.1111/j.1365-246X.2008.03887.x

Kodaira, S., Sato, T., Takahashi, N., Ito, A., Tamura, Y., Tatsumi, Y., & Kaneda, Y. (2007). Seismological evidence for variable growth of crust along the Izu intraoceanic arc. *Journal of Geophysical Research*, *112*(B5). https://doi.org/10.1029/2006jb004593

Sandanbata, O., Kanamori, H., Rivera, L., Zhan, Z., Watada, S., & Satake, K. (2021). Moment tensors of ring-faulting at active volcanoes: Insights into vertical-CLVD earthquakes at the Sierra Negra caldera, Galápagos islands. *Journal of Geophysical Research, [Solid Earth]*, *126*(6), e2021JB021693. https://doi.org/10.1029/2021jb021693